Numerical Analysis of Water Coning for the Recovery of Petroleum: an Enriched BEM Approach

JOSE ANTONIO MARQUEZ-RUIZ

Numerical Analysis of Water Coning for the Recovery of Petroleum: an Enriched BEM Approach

José Antonio Márquez Ruiz

Thesis submitted towards the
degree of Master of Science

Department of Engineering
Durham University
United Kingdom

January 2021

Numerical Analysis of Water Coning for the Recovery of Petroleum: an Enriched BEM Approach

Abstract

The scope of this thesis focuses on enrichment techniques applied to the water coning problem, a numerical simulation solved with the enriched Boundary Element Method (BEM) for potential problems. The problem consists on a time dependent two-zone model with a pumping sink causing the extraction of hydrocarbons. A time dependent two-zone model implicates a moving interface between the zones and since a numerical simulation is performed, a refined discretization of the interface is necessary thus a high amount of Degrees of Freedom (DoF) are needed for its solution. Enrichment schemes reduce the numbers of DoF on the interface, in theory optimising computer effort. The Boundary Integral Equation (BIE) solved for this problem. In this work, the physical aspects of the model and the enrichment scheme are described in order to perform tests that would result in the best enrichment function possible that captures reliable results regardless of the conditions of the model. The enrichment scheme is compared to the classical (unenriched) BEM that is used as a reference solution. The change of scheme results in achieving the same accuracy with 8% of the original number of equations. The results allow us to predict the computational improvements that might be achieved when this technique is applied to 3D or the conditions of the model change. These results suggest that simulations would be over 20,000 times faster without loss in accuracy. This presents industry with a strategy to prevent water to be drawn into an oil well, eliminating an expensive oil-water separation process.

Declaration

The work in this thesis is based on research carried out in the Computational Mechanics Group, Department of Engineering, Durham University. No part of this report has been submitted elsewhere for any other degree or qualification and it is all my own work unless referenced to the contrary in the text. Parts of this work have been published in the following:

Conferences

CONFERENCE
Oral Presentation, 'ENRICHED BEM FOR WATER CONING - 12TH UK BOUNDARY INTEGRAL METHOD'S CONFERENCE' Paper submitted to proceedings.

Acknowledgements

This research would not have been possible without the funding assigned by the National Council of Science and Technology 'CONACYT' in collaboration with the Ministry of Energy 'SENER' and the Federal Government of Mexico; for which I am sincerely grateful. In the same way, special thanks to my supervisor, Professor Jon Trevelyan from the Department of Engineering at Durham University for his great deal of patience, impeccable guidance, and unconditional support.

Thanks extended to Professor Eder Lima Albuquerque from the University of Brasilia and Bohan Chen from University of Oxford, who have set a guide for this research. As well as lecturers, colleagues and staff at Durham University, specially Dr Panos Gourgiotis from the Engineering Department, for his guidance and support in this research; Dr Fiona O'Caroll from International Office for her assistance at Durham; Mrs Evelyn Tehrani and Professor Douglas Halliday from the Durham Energy Institute; Dr Will Coombs and Dr Rui Carvalho whom kindly allowed me to attend to their lectures; Benjamin Gilvey and Fernando Loyola from my research group who helped me when I needed support.

Finally, thanks to the support of Trevelyan College, Durham Students' Union and Durham Mexican Society.

José Antonio Márquez Ruiz
Durham, January 2021

Contents

List of Figures

List of Tables

Acronyms

BEM	Boundary Element Method
BIE	Boundary Integral Equation
BIM	Boundary Integral Method
FEM	Finite Element Method
DoF	Degrees of Freedom
PDE	Partial Differential Equation
RHS	Right-hand side
LHS	Left-hand side
BC	Boundary condition
PUFEM	Partition of Unity Finite Element Method
PUBEM	Partition of Unity boundary element method
PUM	Partition of Unity Method
ACP	Additional Collocation Point

Chapter 1

Introduction

This work is the study of enrichment techniques in the Boundary Element Method (BEM) for potential problems. The model in this project resembles an oil reservoir containing two fluids, oil and water; where a pumping sink in the oil zone forces the oil to be drawn out of the reservoir in consequence of a drop in pressure (i.e. difference in potential), occurring a moving interface problem. An enrichment scheme is appropriate on some of the elements in the interface, as this is the "boundary" that moves when the pumping sink is active and a re-mesh is required for every time step evaluated. Typically, a numerical simulation requires a model to be discretized (i.e. divided into elements) in order for the differential equation can be solved subject certain Boundary Conditions. This creates an algebraic matrix of equations to be solved. The Finite Element Method (FEM) has been for many years the most popular option for the study of mechanics. This method consists on discretizing the physical model to be analysed resulting on a mesh where it is easier perform calculations of change for any material caused by stress. However, a method like FEM discretizes the entire volume of the model, whereas BEM focuses only on the boundary, resulting on a smaller system and causing a re-mesh process to be trivial. In another perspective, this also aids in the matter of computational efficiency. Enrichment functions on an oil-water moving interface have been successfully produced on a specific model, the goal for this research is to obtain an enrichment scheme that achieves the same level of accuracy with 8% of the number of equations. The model is studied in 2D to prove the effect of the enrichment scheme with different collocation strategies, enrichment functions, physical conditions, and changes in the model's geometry. The enrichment scheme is compared to the classical (unenriched) BEM as a reference solution. The results allows to predict the computational improvements that might be achieved when this technique is applied to 3D. The results suggest that simulations would be over 20,000 times faster without loss in accuracy. This presents industry with a strategy to prevent water to be drawn into an oil well, eliminating an expensive oil-water separation process, which represents more than half a million Pounds sterling.[1] – If you can't measure it, you can't improve it – Peter Drucker; this quote has a lot of meaning when it comes to business and science.

1.1 About this work

The physics of the problem is explained in Chapter 2 where an brief explanation of the oil reservoir properties followed by the birth of the concept of the 'Water Coning Phenomenon' in the petroleum industry and its previous studies finalising with the latest studies on the subject. Here, Darcy's law leads to conclude the governing equations of the problem where a potential causes the fluid to flow with a

[1] Calculated 1 million Australian Dollar to Pound sterling equals £ 535,379.20 05 November 2019 google.com

gradient given by the the flux density. Also the geometry of the problem and its physical conditions are defined and described. The BEM is described step by step on chapter 3 where the Boundary Integral Equation (BIE) is conformed and regularised. This method becomes attractive to the author as the BIE drops dimensionality to work only with boundaries and enabling the model to focus on the moving interface. The enrichment approach is described in chapter 4. The core of the present work lies within the enrichment of the BEM as one of the main goals is the reduction of the number of Degrees of Freedom (DoF) maintaining accurate results by capturing the behaviour of the potential and flux density on the interface. This idea of enrichment is originated by the previous Partition of Unity Method (PUM) and Partition of Unity Finite Element Method (PUFEM). As mentioned at the beginning of the current chapter, for everything that the author wishes to improve, metrics and indicators are vital for this research. A description of these metrics is included, where a) Total flux on the interface and b) the Relative error of the $L2$ norm are the main ones. This last one requires a reference solution which is obtained from a refined traditional BEM model. This research features a series of tests performed in order to achieve the best strategies and modifications to the enrichment function and model to ensure fidelity for most condition changes. The full simulation of the water coning problem would require a multiphysics approach, in which gravitational effects interact continuously with fluid dynamics through porous media as driven by a pumping sink. This might be solved using the Navier-Stokes fluid equation. However in this initial study we will simplify the problem by a pseudostatic approach in which the fluid dynamics is expressed using the Poisson equation, and the consideration of gravitational effects will be left for a future project. This is because the focus of the research is on the use of different approximation spaces to capture the flux density efficiently, and the flux distribution is expected to be well approximated by the solution of the Poisson equation. Specifically, the aim of the research is the exploration of schemes by which the potential flow analysis using the BEM can be 'enriched' in order to achieve better approximation properties for this problem, thereby enabling accurate results to be obtained from much coarser meshes than have been possible using classical BEM formulations using conventional piecewise polynomial elements. Strategies like a different array on collocation points, changes on the flux density enrichment function are assessed and the best resulting strategy is selected. The numerical evaluation is performed using the Gauss-Legendre Quadrature, where different Gauss points are also analysed. Physical changes to the model are described and carried out to ensure consistency on the approach's accuracy. Finally chapters 5 and 6 conduct a discussion on the resulting effects of the tests performed and a conclusion of the project.

1.2 Publication

The following publication arose from this work:

J. M. Ruiz, B. Chen, J. Trevelyan, P. Gourgiotis, E. Albuquerque, and C. U. D. Ribeiro, "Enriched bem for water coning," *Methods UKBIM12*, p. 41, 2019

The author was first author on the paper and wrote much of the introductory material and engineering interpretation, though the formulation tested was the work of B. Chen.

1.3 Novel contributions

The novel contributions contained in this thesis include:

- Enriched simulation in water coning
- Multiple candidate enrichment functions are tested and optimal functions are selected
- Effects of oversampling are investigated
- Effects of different pump location are investigated

- A simulation on different geometry is implemented
- Performance indicators for the model are introduced ie. Total flux and Relative Error or the L_2 Norm

Chapter 2

Water Coning Problem

A confined aquifer consists of a homogeneous or inhomoheneous fluid (ground water) restricted between permeable layers. Its behaviour is governed by the theory of fluid mechanics. Porous media are defined as solid spaces also known as 'solid matrix' with interconnected pore spaces, ie. void spaces in between. Void spaces in solid matrices are saturated with fluids, usually water and some times hydrocarbons in a gas or liquid form as a result of organic residue from early geological times according to 'The organic theory'. This is the theory most accepted by scientists that explains how animal and plants from early ages were trapped in 'source beds' and then leaked over time into porous rocks [4].
Oil, or 'crude' as it is commercially known, lies in porous rock formations called 'oil reservoirs' usually formed of limestone, sandstone or dolomite. Oil reservoirs are found in the underground varying from 90 up to 1200 metres below ground level. These porous media are composed of two impermeable layers on top and bottom similar to a confined aquifer according to Bear [4]. Between these permeable layers, the pore space is fully saturated in equilibrium with water in a range from 2% and 50% of the pore space and the rest with hydrocarbons in a liquid (oil) or gas form [5].

For the purpose of this simulation and analysis, oil and water are the only fluids considered. As oil is the lightest by having a lower density, water can be found in the bottom section of the reservoir leaving oil on top. This effect produces a theoretical line called interface Γ_{ow} which is where both fluids intersect, making this a two-zone problem. Considering both fluids to be immiscible, this interface is considered to be sharp [4].

In his book, Muskat [5] briefly explains the oil recovery process which consists of an ensemble of wells drilled until they reach an oil-water reservoir as previously described. A duct is introduced through the ground and a sink is fixed in the zone where the oil is found. When the mechanism is active, the oil surrounding the sink is drawn in first; in consequence at the same time water in the zone below the interface is drawn towards the pumping sink as well. This occurs due to the difference of densities and viscosity of the fluids. The surface of the water drawn towards the pump forms a cone-like shape where the 'Water Coning Phenomenon' obtains its name [6]. It is ideal to achieve the maximum pumping rate for recovery, where the interface maintains equilibrium. When the equilibrium is broken and the interface reaches the pumping sink, the two liquids are mixed and in consequence, a further separation process has to be performed later.

2.1 Previous studies

Early studies from 1934 show that Muskat et al. [6] introduced the concept of Water Coning in the oil production industry. In their work, the fundamental physical principles underlying the water-oil interface when the pumping sink is introduced partially in the zone of extraction (oil zone) are presented. They concluded that a) as the interface reached 50 to 75 percent of the height towards the sink, an accelerated increase in the rise rate of the interface was presented producing instability and extreme sensitivity on the interface to small changes in the oil recovery rate; b) Oil cannot be produced without water when the oil zone is particularly thin, unless the recovery rate was reduced to be non profitable; c) Clearly it is not recommended to penetrate very close to the water zone, but for any given depth of the oil zone a minimum penetration of 15 to 20 percent allows the maximum production rate of the oil without water; d) Unless it is plugged back to an impermeable lens, it is ineffective to plug back a well that has a small penetration already; e) The best method of control is to rapidly increase the recovery rate to its optimal capacity rather than slowly reaching that point because there is a possibility of a prominent hysteresis in the curve of pumping rate (pressure differential) against interface height; And finally f) for a given average pumping rate a steady flow will yield a lower interface height as opposed to an intermittent flow.

Based on Muskat's theories, Høyland et al. [7] in 1989 developed an analytical model and validated against a range of finite difference simulations. It was not until 1991 that Lucas et al.[8] presents a study of the steady-state shape of the water coning with a Boundary Integral Method (BIM). In their work, a brief explanation on the water coning phenomenon was described and how the Darcy's law may be applied in on fluid movement in porous media in a macroscopic level. In the case of fluid movement in porous media using relative permeability and saturation often suffer instabilities near the well requiring restricted time steps or application of Boundary conditions at some distance from the well; mainly due to the vastly increasing flow rate of fluid as it approaches the sink or well [9]. The interface used in [8] resembles a 'cusp' [10], which in a mathematical sense, is described as a singular point of a curve where the limits of tangents approaching from either side coincide. This shape is the limiting shape of the interface, any higher flow rates will lead to a breakthrough of the water into the well. Lucas et al. in their first paper [8] focus on the steady-state problem reaching a concussion where they developed a BIM which predicts the steady-state height of the interface between oil and water in an oil-water reservoir under the influence of an oil recovery well obtaining the most straightforward model for a numerical solution on critical flow rates. Later studies from Al-Alfeg and Ershaghi 1993 [11] consider water coning in naturally fractured reservoir; issues of critical rates and time for water to reach the sink. They proposed a time correlation to account for fracture acceleration effects against uniformly distributed fractures studying fracture distributions; and conclude that the estimation of critical rate requires an understanding of fracture patter around the producing wells.

In 1998, Lucas and Kucera [12] explored the problem with the studies of numerical analyses for various general multi-sink distributions instead of the previous asymmetric single well problem [8]. Sophisticated integration techniques are implemented in an effort to obtain accurate results, particularly the efficiency of various integration method are compared for this problem. In a complementary way, they were the first on assessing the problem in 3D. In their conclusions, they achieved the developed a BIM which determines the steady state height of the oil-water interface under the influence of a distribution of oil production wells. However, they faced an obstacle regarding the CPU time required to be significantly larger compared to the axisymmetric single-sink problem. Further studies were conducted by Farmen et al. in 1999 [13] regarding the dynamics of the water coning through experiments achieving a stochastic simulation of the invasion percolation type. This work already considers a time-stepping measure to study

the moving interface problem that characterises water coning. Another study from Bahrami et al. [14] was assessed regarding physical changes of the reservoir and well, where breakthrough time sensitivity and water cut were tested on different fracture and matrix permeability (horizontal and vertical) were tested; concluding that breakthrough time is more sensitive to horizontal and vertical fracture permeability and water cut is more sensitive to horizontal fracture and matrix permeability. A recent study by Perez et al. [15] in 2012 performs a simulation of a porous fracture system based in the Mexico Bay of Campeche. Their goal was to recover the remaining hydrocarbon from the reservoir and found necessary to find the optimal operation range minimising the water breakthrough; their approach was to model in detail water coning using a fine radial grid with 1 metre thick layer concentric around the well and 2 inches hick layers in the annulus. This leads to explore an approach where a coarse discretisation may be possible.

More recently in 2015, Azim [16] develops a numerical model based on upstream flux weighted finite element discretisation method combined with single-continuum and discrete fracture approach. The presented 3D multi phase poroelastic numerical model assesses the water coning phenomenon in naturally fractured reservoirs and has the ability to simulate large numbers of discrete fracture in the reservoir domain. A decrease in vertical permeability lead to increase the water cut and water saturation as similar to Bahrami; the decrease of oil production rate leads to decrease of produced water cut; and the aquifer strength has little effect on produced water cut. However the investigation of the effective parameters is vital to understand the physics of the mechanism and helps with simulation.
The Boundary Element Method (BEM) has been explored as well. Gontijo et al.[2] used the BEM to study in 2D the Water Coning Phenomenon and developed a time-stepping scheme in which the moving interface location could be determined by the flux density across the interface. He used simple linear boundary elements, and a refined mesh on the interface was required to capture results with enough accuracy. His model works very well in 2D with a simple geometry, however in 3D it may be more efficient to relax the refinement without compromising accuracy. In 2018 the present author published an enriched BEM formulation [3] approach adding two enrichment functions guided by the work on enrichment by Mohamed et al.[17] in 2014.

The idea of enriched methods has its roots in the Trefftz methods, in which the approximation space is comprised of sets of functions that are themselves solutions to the governing differential equation. Fundamentally, this allows accurate results to be obtained using a small number of degrees of freedom because the approximating functions are chosen to be specific to the space of functions known to make up the solution in some way. The implementations of enrichment in the modern era started with the Partition of Unity Method of Melenk [18], which has spawned a large body of literature. Perhaps the most common of these methods is the eXtended Finite Element Method (XFEM), seen in, for example, Moës et al. [19], in which the focus is the accurate solution of problems in fracture mechanics. The detailed literature review of enriched methods is deferred until the early parts of Chapter 4 of this thesis, where enrichment is introduced.

2.2 Physics of the Water Coning Phenomenon

To describe the physics of the oil reservoir it is fair to say that it is considered to have an homogeneous porous medium. This property is described by constant isotropic permeability k also known as 'coefficient of permeability', which defines the level of porosity of the medium and how well a fluid can move. According to Farmen [13], the pressure distribution in the reservoir is determined by viscous and hydrostatic contribution. During the coning process, the interface conditions at the oil-water interface change,

as both oil and water begin rising. Depending on the flow rate Q $[L^3T^{-1}]$, the cone distribution may reach an equilibrium and will not come into the well; but if the flow rate exceeds critical value, the cone will become unstable occasioning water mixing with oil inside the well. Each of the fluids considered, in this case oil and water have a density value ρ_o $[ML^{-3}]$ for oil and ρ_w $[ML^{-3}]$ for water that determines the weight of each fluid. In the same way they also have a dynamic viscosity of μ_o $[ML^{-1}T^{-1}]$ for oil and μ_w $[ML^{-1}T^{-1}]$ for water which describes the fluid's resistance to flow. Both fluids are considered incompressible, at rest, and stratified by their density. Naturally, the section on top of the interface is composed of oil and the one below of water given as a result of their differences in density as mentioned before. When the pump is active, oil is withdrawn from the oil zone (determined by Ω_o) permanently at a constant rate of Q per unit width. Consider a column of density ρ and of height u above a datum at coordinate $z = 0$. Consider now a point at same non-zero high z above this datum; the hydrostatic pressure, p, at this point due to the portion of the fluid column above it is

$$p = (u - z)\rho g \tag{2.1}$$

where g is the acceleration due to gravity[4]. Rearranging, is found

$$u = \frac{p}{\rho g} + z \tag{2.2}$$

This description shows how the total height of the fluid column, u, may be described in the terms of the pressure at any height z above its base. The variable u may also be described as the piezometric head and, as will be shown, the spatial variation in u is governed by the Poisson equation so it can be thought of as a potential and facilitating its analysis by numerical methods. This is considered to be the energy of a fluid per unit weight and determines the direction in which the fluid will flow when the system is active. This work's model is governed by Darcy's Law, which describes the motion of homogeneous fluids in porous media. The gradient of the potential ∇u is defined as the flux density $\mathbf{q}$ for the $x-z$ directions as it flows on the area Ω and q for the direction normal to the boundary Γ

$$\nabla u = \begin{cases} \mathbf{q} = \left[\frac{\partial u}{\partial x}, \frac{\partial u}{\partial z}\right] & \text{flux is in } \Omega. \\ q = \frac{\partial u}{\partial n} & \text{flux is in } \Gamma. \end{cases} \tag{2.3}$$

2.2.1 Darcy's Law

In his experiments, Henry Darcy studied the flow of water in vertical homogeneous sand filters connected to the fountains of the city of Dijon, France. He concluded that the rate of flow Q $[L^2T^{-1}]$ is (a) proportional to the constant cross-sectional area A (area where the fluid discharges), (b) proportional to the difference of the piezometric head across the filter $(h_1 - h_2)$, and (c) inversely proportional to the length L of the porous media. These conclusions combined produce the world famous Darcy's Law:

$$Q = \frac{KA(h_1 - h_2)}{L} \tag{2.4}$$

where K $[MT^{-1}]$ represents the 'hydraulic conductivity' of the porous media defined by:

$$K = \frac{k\rho g}{\mu} \tag{2.5}$$

Darcy recognises h as the piezometric head (distance from a certain datum to the water head), and $h_1 - h_2$ as the difference of piezometric head across the filter of length l [L]. This difference is the energy

that makes the water flow from higher piezometric head to the lower. More over, Darcy introduced J as 'hydraulic gradient' :

$$J = \frac{h_1 - h_2}{l} = \frac{\Delta h}{l} \tag{2.6}$$

where h is equivalent to z from equation (2.2). In Darcy's experiment, this value is the energy that makes the water move and is called 'potential' u $[L]$. Bear [4] defines 'specific discharge' d $[LT^{-1}]$ as the flow rate Q per unit cross-sectional area A normal to the direction of the flow, and is represented by:

$$d = \frac{Q}{A} \tag{2.7}$$

having defined these concepts, we simplify (2.4) by including (2.6) and (2.7) to obtain another simplified model for the Darcy's Law:

$$d = KJ \tag{2.8}$$

notice that this model is limited to one-dimensional flow. In the case of oil recovery in a 2D model of an oil reservoir in the $x - z$ plane, the hydraulic gradient J must be treated as a vector:

$$-\nabla u = \mathbf{J} \equiv [J_x, J_z] \equiv \left[\frac{-\partial u}{\partial x}, \frac{-\partial u}{\partial z}\right] \tag{2.9}$$

where $J = -q$ due to the fact that the flow goes through the regions of high potential to low potential; and therefore so does the vector $\mathbf{d}$:

$$\mathbf{d} \equiv [d_x, d_z] \equiv \left[\frac{-K\partial u}{\partial x}, \frac{-K\partial u}{\partial z}\right] = K \cdot -\nabla u \tag{2.10}$$

known as specific flux vector. When the hydraulic conductivity K $[MT^{-1}]$ multiples the potential u this results to be the velocity potential $\mathbf{v}$:

$$\mathbf{v} = Ku \tag{2.11}$$

2.3 Geometry

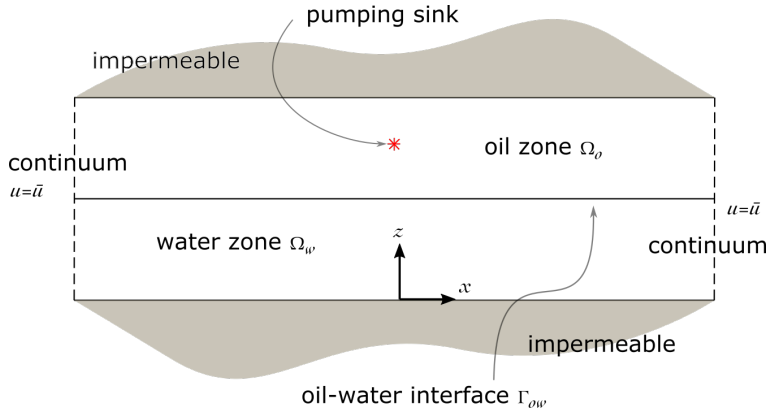

Figure 2.1: Basic Geometry of the Water Coning Model

The problem is originally modelled with a basic rectangular geometry of a single porous medium Ω. When saturated by two different fluids this medium is composed by two zones as shown in figure 2.1, the two immiscible fluids that meet each other are defined as Ω_o for the oil zone as mentioned earlier and Ω_w for the water zone. According to Bear [4] the formed interface defined by Γ_{ow} is considered to be

sharp due to the immiscibility of the fluids. This assumption makes this a two zone problem, which is treated in the x—z plane. The top and bottom boundaries of the model are impermeable by definition, and are considered to be spaced 4 metres from each other. For this model each zone is equally distant from the interface to their top and bottom boundaries ie. both zones are 2 metres thick. This means that the interface of the zones Γ_{ow} is set to be the same height in the z plane for simulation purposes in a first set of tests. This later is slightly changed to test the reliance of the model in a more realistic approach. The side boundaries' extension reaches a point far enough causing the effect of the pump to be negligible. In the current work, the side faces of the problem spaced 20 metres from each other, the same as that adopted by Gontijo [2]. A pump is located in the oil zone since this the zone for extraction. The pumping sink in this model is located in the middle of Ω^o (oil zone), where it is not particularly close to the interface but also high enough to obtain as much oil as possible.

It was explained in Chapter 1 that the focus of the current work is the accurate and efficient Boundary Element simulation of the pseudo-static case, and specifically the use of enrichment to efficiently resolve the flux density distribution on the interface. The case of equal densities $\rho_o = \rho_w$ is therefore considered for simplicity. However, it should be noted that where the oil and water densities are different, the physical requirement for continuity of pressure p across the interface means that the potential u must become discontinuous. So the Dirichlet boundary conditions on the left and right faces of the model shown in Figure 2.1 could be replaced by $u = \bar{u}_o$ and $u = \bar{u}_w$, respectively, on the upper and lower portions of these lines.

In his work, Gontijo et al. [2] gives three key statements (a) To allow the analysis of the Water coning phenomenon in two zones, it is essential to know the position of the oil-water interface when pumping is active; (b) The calculated flux at the interface is the velocity of the fluid that defines it i.e. **d** from equation (2.8); and (c) Introduces

$$\frac{\partial \eta}{\partial t} = -\frac{K}{\theta} q_m \Delta t \sqrt{1 + \left(\frac{\partial \eta}{\partial x}\right)^2_m} \tag{2.12}$$

where θ is the medium porosity, $\eta(x,t)$ is the function that expresses the height of the interface at a given x coordinate and a given time, to define the height variation of a given node of the interface in the simulation of the interface movement at 'time step' m of size Δt. To implement this, equation (2.12) is re-written in therms of finite differences

$$z_{m+1} = z_m - \frac{K}{\theta} q_m \Delta t \sqrt{1 + \left(\frac{\partial \eta}{\partial x}\right)^2_m} \tag{2.13}$$

where z is the height of the elevation at present time step and the immediately next one m and $m+1$ respectively.

2.3.1 The Laplace and Poisson Equation

For this work, the two materials to be analysed are oil and water, both incompressible fluids i.e. liquids, both with a constant density and fluid viscosity. Thus the explanation is focused on them.
In their book, Zienkiewicz et al. [20] explain that any material's behaviour is governed by the stress acting upon it. The difference between a fluid and a solid is that a fluid in rest cannot sustain any deviatoric stress. Thus, only pressure or a compressive stress (in the case of compressible fluids) can be applied. In reference to liquids, this pressure is the same as the hydrostatic stress, which is a normal stress. For any

analysis of a fluid to be relevant, this last one has to be in motion, and here is where a deviatoric stress can develop. This will be characterised by a quantity called dynamic viscosity μ which is the equivalent to the shear modulus in solid mechanics. In solid mechanics, the displacement is represented with the vector $\mathbf{u}$, this is replaced in fluid dynamics by the velocity vector represented often in the same way.
A potential (2.2) is the reason for any fluid to flow, and the velocity of the flow is the main characteristic that is studied in fluid dynamics [4]. Thus, this is referred to as the velocity potential. Unless we are dealing with a highly compressible fluid, conservation of mass is always necessary when a fluid is in motion, therefore we require the divergence of the velocity vector to be zero. Assuming a change of densities, the mass conservation is defined as the balance of mass flow $\rho\mathbf{u}$ is equal to the rate of change in density when entering and leaving an infinitesimal control volume resulting in the continuity equation:

$$\frac{\partial \rho}{\partial t} + \nabla(\rho \mathbf{u}) = 0 \tag{2.14}$$

however, when an incompressible flow is treated, the density ρ is constant. In this case, the mass conservation energy is simplified:

$$\nabla \mathbf{u} = 0 \tag{2.15}$$

replacing $\mathbf{u}$ from (2.9) into (2.15):

$$\nabla \cdot \nabla u = \nabla^2 u = 0 \tag{2.16}$$

obtaining the Laplace equation. When the pumping sink is inactive, this equation governs the whole geometry. When the pumping sink is active, the strength of the pump $S \neq 0$, the Laplace equation still applies in the water zone Ω_w; on the other hand, the oil zone Ω_o is now governed by the Poisson equation [13]:

$$\nabla^2 u(\mathbf{x}) = S(\mathbf{x}), \qquad \mathbf{x} \in \Omega_o \tag{2.17}$$

Here, S is a general source term that may apply to any spatially varying form of source (if $S < 0$) or sink (if $S > 0$). However, for the simpler case of a point source (or sink), such as at the situation modelled in the water coning problem driven by a pump at point, we can describe the source term as

$$S(\mathbf{x}) = Q\Delta(\mathbf{x} - \bar{\mathbf{x}}) \tag{2.18}$$

Where Δ is the Dirac delta function, $\bar{\mathbf{x}}$ denotes the location of the pumping source and Q describes the pumping strength. It is worth noting that using this description of the form of S is particularly helpful for boundary element implementation as it precludes the need to evaluate a volume integral that would otherwise arise.

2.3.2 Boundary Conditions

For this particular problem, the potential u and the flux density q are known in all of the geometry as long as the pumping sink is inactive. Once the system is in operation, the pressure at the source will drop, moving the interface and the values in the geometry will change.
As it has been established before in Section 2.3, the boundaries in the $z-$axis i.e. lateral boundaries are far enough from the sink for this to have any significant effect, thus the potential at these points will remain the same $u = \bar{u} = 4$. In the same way, top and bottom boundaries are formed of impermeable rock, thus no flow occurs there $q = 0$.
In a boundary value problem like this, the 'fixed' values ($u = \bar{u} = 4$), also known as the *Dirichlet* Boundary conditions (BCs) are one of the different types of boundary conditions in Partial Differential Equations (PDEs). A common alternative is where the derivative of this condition is given. This is called

the *Neumann* Boundary conditions (BCs), in this case the derivative of the potential is the flux density which at the top and bottom boundaries, the impermeable property of the material does not allow flow i.e. $q = 0$ [4, 21].

Chapter 3

Boundary Element Method

In the previous chapter an explanation of the physics of the problem has been covered and how this leads to the governing equations of the two physical zones. It is now appropriate to describe the method employed to solve the whole system of equations and the steps to do so. In this work we adopt the Boundary Element Method (BEM) and this chapter presents the classical BEM formulation in a standard direct collocation as shown in many text books.

The classical Laplace equation (2.16) is a partial differential equation. The problems that are governed by it can be solved through various methods, but the most common method to solve this is the Finite Element Method (FEM) eg. [21, 22]. While the FEM offers engineers a versatile solution capable of solving a wide variety of problems, the specific water coning problem is of a character that is better suited to the BEM. The principal reason is that this is a moving boundary problem, since the interface between the oil and water zones moves between each time step in response to the calculated flux density across it. This is efficiently handled by the BEM since the required re-meshing is a trivial process. We also benefit from a reduction in the size of the system in comparison to FEM. Figure 3.1 from Trevelyan [1] shows a diagrammatic representation of a typical FEM stiffness matrix (in reality the matrix is unlikely to be rigidly banded like this, but will be diagonally dominant and sparse). The BEM system, while fully populated, is considerably smaller and likely to contain far fewer non-zero entries. Thus a fully populated matrix cannot be seen entirely as a disadvantage. This conclusion was also reached by Gontijo [2] for the water coning problem. Importantly also, the BEM scheme allows us to define a simpler enrichment scheme, to be described in the following chapter.

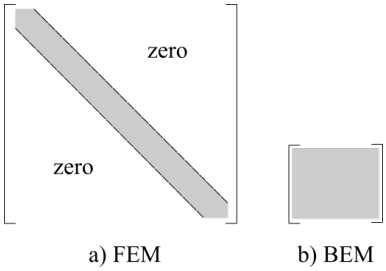

Figure 3.1: System matrices from Trevelyan [1]

3.1 BEM for potential problems

With a physical problem established and having defined a governing equation, a numerical implementation is to be in place where four steps are to be undertaken to solve the system: a) discretization; b) numerical integration; c) application of the Boundary conditions (BCs); and finally d) solution of the algebraic equations as suggested by Becker [23]. An additional step is also described e) calculation of the internal variables; but for the purpose of this work, this is not required. This method can be applied to potential problems, where potential can be the temperature of a body on a heat transfer problem, or the voltage in an electric problem. To solve any differential equation in the BEM, a fundamental solution equation is key. For the Laplace equation, the fundamental solution is as follows

$$u^*(p,Q) = \frac{1}{2\pi} \ln\left[\frac{1}{r(p,Q)}\right] \tag{3.1}$$

where u^* is the potential at the 'field point' p that arises as a result of a source point at Q; in the same way $r(p,Q)$ is the distance between these points where the point or 'node' on the element is that is being evaluated. This distance is represented by

$$r(p,Q) = \sqrt{(X_p - x_Q)^2 + (Z_p - z_Q)^2} \tag{3.2}$$

where X_p and Z_p represent the coordinates of the load point and x_Q and z_Q represent the coordinates of the field point. In fluid dynamics, it has been established the potential u as (2.2) and the flux density q as the potential's gradient, given by the partial derivative of the potential with respect of a point in the plane. The terms derived from the fundamental solution are called the 'kernels' u^* and q^*. In this text they can be identified as the terms with the star as a superscript. These equations will be fundamental to the Boundary Integral Equation (BIE). Another important fact to be noted is that the fundamental solution is 'singular' i.e. becomes infinite as the distance r approaches to zero; this complicates the evaluation of the boundary integrals required in the implementation of the BEM. In this case, a regularisation scheme is to be implemented over other methods, this is discussed later in the chapter.

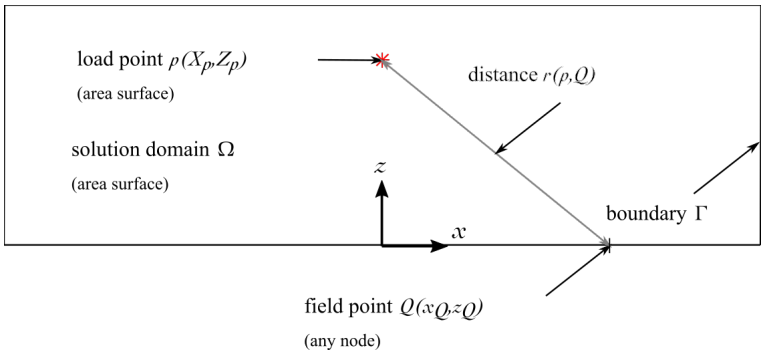

Figure 3.2: 2D physical domain model

3.1.1 Boundary Integral Equation

The most important aspect of this method, contrary to FEM, is that the BEM formulation drops the dimensionality of the problem to work only with the variables on the boundary rather than the ones in all of the area. This is possible in two steps: firstly applying the divergence theorem

$$\int_\Omega \nabla \cdot \mathbf{f} \; d\Omega = \int_\Gamma \mathbf{f} \cdot \mathbf{n} \; d\Gamma \tag{3.3}$$

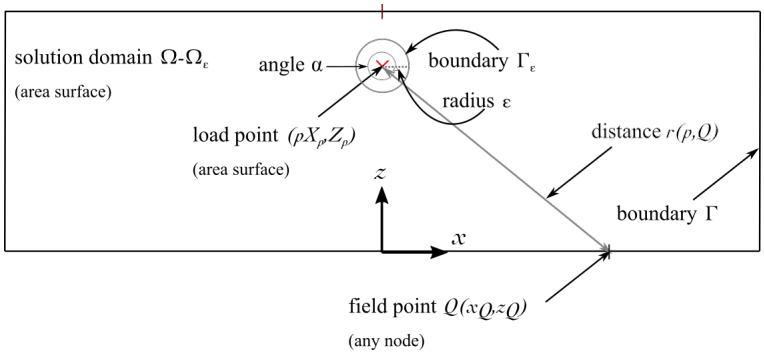

Figure 3.3: 2D physical domain model with ϵ boundary

where an arbitrary function **f** has continuous first derivatives with respect of the Cartesian coordinates and **n** represents the unit outward normal vector; and secondly moving the internal load point p to the boundary where it will be renamed as P. Equation (3.3) is also known as Green's theorem in honour to the British mathematician George Green. This theorem has other forms, and for this particular problem it is appropriate to use Green's second identity; where we assume the existence of two variables with continuous first and second derivatives within the area

$$\int_\Omega \left(u\nabla^2 u^* - u^*\nabla^2 u\right) \ d\Omega = \int_\Gamma \left(u\frac{\partial u^*}{\partial n} - u^*\frac{\partial u}{\partial n}\right) \ d\Gamma \tag{3.4}$$

where u and u^* are not arbitrarily chosen; u is the unknown potential at any point and u^* is the fundamental solution to the Laplace equation; $\partial/\partial n$ is the derivative of the functions in direction of the outward normal vector. The potential function u satisfies the governing equation i.e. Laplace equation $\nabla^2 u = 0$ everywhere in the solution domain by definition. However, the fundamental solution u^* satisfies $\nabla^2 u^* = 0$ but when the field point becomes the load point, a singularity is produced. According to Becker [23] it is appropriate to imagine a circular perimeter surrounding the load point p with a diameter of ϵ. This way, on the LHS of equation (3.4) by definition $(\Omega - \Omega_\epsilon)$, $\nabla^2 u = 0$ and$\nabla^2 u^* = 0$ ie. the whole LHS is equal to 0, however, the RHS equals the summatory of the integrals of the boundary Γ minus the inside of this circle plus the area of the circle Γ_ϵ. ϵ

$$0 = \int_{\Gamma-\Gamma_\epsilon} \left(u\frac{\partial u^*}{\partial n} - u^*\frac{\partial u}{\partial n}\right) \ d\Gamma + \int_{\Gamma_\epsilon} \left(u\frac{\partial u^*}{\partial n} - u^*\frac{\partial u}{\partial n}\right) \ d\Gamma \tag{3.5}$$

Notice that the volume integral was removed on the basis that the Laplace equation is satisfied. However, in the oil zone this is not the case and the Poisson equation (2.17) governs the problem. Discussion of this is deferred until Subsection 3.2.2. After having the integral split, the first part of the integral becomes weakly singular as the field point Q does not come close to the load point p. The second term in equation (3.5) is strongly singular as the field point becomes closer to the load point. To deal with this singularity, Becker [23] uses the Chain rule to adapt the integral of Γ_ϵ with an angle α at point p anticlockwise as shown in figure 3.3 to substitute $d\Gamma = \epsilon \ d\alpha$

$$\frac{\partial u^*}{\partial n} = \frac{\partial u^*}{\partial r}\frac{\partial r}{\partial n} = \frac{1}{2\pi}\frac{(-1)}{r}(-1) = \frac{1}{2\pi r} \tag{3.6}$$

now it is integrated to the limit as $\epsilon \to 0$ within the limits of α from 0 to 2π. The second integral of

(3.5)becomes

$$\begin{aligned}\int_\Gamma \left(u\frac{\partial u^*}{\partial n} - u^*\frac{\partial u}{\partial n}\right)\ d\Gamma &= \frac{1}{2\pi}\int_0^{2\pi}\left[u\left(\frac{1}{\epsilon}\right) - ln\left(\frac{1}{\epsilon}\right)\frac{\partial u}{\partial n}\right]\epsilon\ d\alpha \\ &= \frac{1}{2\pi}\int_0^{2\pi}\left[u + (\epsilon ln\epsilon)\frac{\partial u}{\partial n}\right]\ d\alpha \\ &= \frac{1}{2\pi}\int_0^{2\pi}(2\pi u) \\ &= u(p)\end{aligned} \tag{3.7}$$

and equation (3.5) becomes

$$u(p) + \int_\Gamma q^*(p,Q)\,u(Q)\ \ d\Gamma(Q) = \int_\Gamma u^*(p,Q)\,q(Q)\ \ d\Gamma(Q) \tag{3.8}$$

where $q = \frac{\partial u}{\partial n}$ and $q^* = \frac{\partial u^*}{\partial n}$.
The point p is still in the internal area rather than the boundary as Figure 3.2 represents. In this case, p is moved to the boundary and is referred now as P resulting the following equation

$$C(P)\ u(P) + \int_\Gamma q^*(P,Q)\,u(Q)\ \ d\Gamma(Q) = \int_\Gamma u^*(P,Q)\,q(Q)\ \ d\Gamma(Q) \tag{3.9}$$

where the coefficient $C(P)$ represents the proportion of the potential in the 'fictional' load point on the interface, usually $\frac{1}{2}$ e.g. if the point were inside the volume then $C(P) = 1$ and if this were outside the solution domain, $C(P) = 0$.

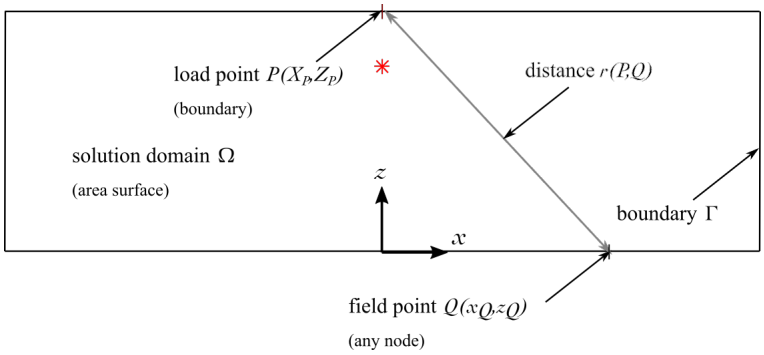

Figure 3.4: 2D physical domain model with boundary-only points

Another way of dealing with the singularity caused in (3.5) is to regularise the equation which is explained later in this chapter.

3.2 Solution

To solve equation (3.9) in a geometry of any shape, numerical integration has to be performed and this requires discretizing the geometry of the physical problem in small 'boundary elements'. Each element is defined by nodal points N i.e. nodes, each of which has coordinates (x,z) to define the geometry of the element and also has variables describing the potential and flux density at the point. In the case of linear elements these are only two and each node has two variables: potential u and flux density, q thus for a problem that is discretized using N nodes there will be $2N$ variables. As will be seen, in order to arrive at a square system of equations that allow us to proceed to a solution, at every node there should be a prescribed variable that can be either u or q and usually come from the Boundary Conditions; which means that there is left N number of unknowns. We therefore need N equations to be able to solve the

system, and this is usually achieved by considering (3.9) N times by placing point P at each of the N nodes in turn. As it was mentioned at the beginning of this chapter, there are five stages or steps that are to be undertaken for the method to work.

3.2.1 Step 1: Discretization

The boundary Γ of the solution domain is discretised into a number of elements that are connected between each other; the last node of an element becomes the first of the next one and so on. For every element, an order in variation of the geometry is in place and these can be linear, quadratic, cubic or another order; obviously increasing the order of the variation of an element increases the accuracy of the solution, but also increases the number of Degrees of Freedom (DoF) i.e. the equations to solve consuming more CPU time. Becker [23] in his book states that previous experience in BEM and FEM for this variation the best approach to have the most efficiency in CPU time and accuracy is the use of quadratic isoparametric elements; however, linear elements will be sufficient for this work in view of (a) linear elements generally perform well for potential flow problems, and (b) Gontijo [2] used linear elements; the use of the same element order will allow a more scientific comparison.
The behaviour of an element is best described in a form of 'shape functions'; they use a number of nodes in each element where the variable value is given. Shape functions will need to have their own coordinate system with origin at the midpoint of the element and values of -1 and 1 at the end nodes. This new coordinate system uses a new intrinsic variable ξ. Now the geometry of the element is described by the coordinates of its nodes and the shape functions. Since the shape functions are isoparametric, the same shape functions are used for the solution variables yielding

$$u(\xi) = \sum_{c=1}^{2} N_c(\xi) u_c = N_1(\xi) u_1 + N_2(\xi) u_2 \tag{3.10}$$

$$q(\xi) = \sum_{c=1}^{2} N_c(\xi) u_c = N_1(\xi) q_1 + N_2(\xi) q_2 \tag{3.11}$$

where each node's function N_c is by definition

$$\begin{aligned} N_1(\xi) &= \frac{-\xi}{2}(1-\xi) \\ N_2(\xi) &= \frac{\xi}{2}(1+\xi) \end{aligned} \tag{3.12}$$

so that the shape functions exhibit both the Kronecker delta and partition of unity properties.

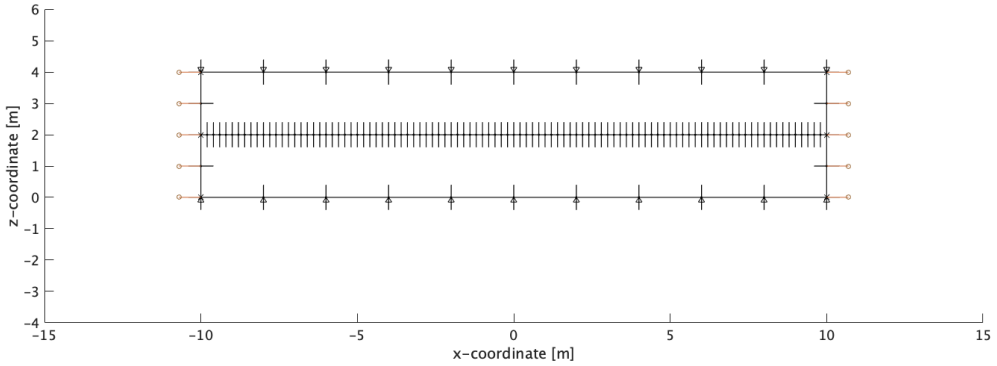

Figure 3.5: Discretized reservoir with 50 elements along the interface from Gontijo [2]

The discretisation leads us to the concept of a boundary element mesh showing the individual elements used in the simulation; an example mesh for the problem under consideration is shown in Figure 3.5 [2].

3.2.2 Step 2: Numerical integration

The Gauss-Legendre quadrature technique for numerical integration is based on an interval $-1 < \xi < 1$ and this fits well with the range of the parametric variable ξ over each element. The numerical integration is performed over each element in the local coordinates of ξ rather than the global boundary coordinate system (x, z). In order to execute an integration in another coordinate system, a 'transformation' of the variable from the boundary Γ to the intrinsic coordinate ξ is to be performed firstly. To do this, the Jacobian $J(\xi)$ is employed resulting a new equation

$$C(P)\, u(P) + \sum_{e=1}^{E} \sum_{c=1}^{2} u(Q) \int_{-1}^{1} q^{*}\left(P, Q\right) N_c\left(\xi\right) J\left(\xi\right) \quad d\xi = \sum_{e=1}^{E} \sum_{c=1}^{2} q(Q) \int_{-1}^{1} u^{*}\left(P, Q\right) N_c\left(\xi\right) J\left(\xi\right) \quad d\xi \tag{3.13}$$

where E is the total number of elements.
A set of linear algebraic equations $A_{e,c}$ and $B_{e,c}$ can be arranged by lumping together the integral functions containing the kernels leaving

$$C(P)\, u(P) + \sum_{e=1}^{E} \sum_{c=1}^{2} u(Q) A_{e,c}\left(P, Q\right) = \sum_{e=1}^{E} \sum_{c=1}^{2} q(Q) B_{e,c}\left(P, Q\right) \tag{3.14}$$

This way a set of linear algebraic equations can be formed and treat each node in turn as the load point P and perform the respective integrations from (3.13). This results on the following matrices

$$\mathbf{Au} = \mathbf{Bq} \tag{3.15}$$

At every node, the integrals of the fundamental solutions u^* and q^* multiplied by the shape functions produces

$$\begin{aligned} RHS \rightarrow \int_\Gamma u^* \left[N_1 \; N_2\right] \; d\Gamma \quad & \begin{Bmatrix} q_{Q1} \\ q_{Q2} \end{Bmatrix} \\ = \left[g_{P,Q1} \; g_{P,Q2}\right] \quad & \begin{Bmatrix} q_{Q1} \\ q_{Q2} \end{Bmatrix} \\ = \left[g_{P,Q1} q_{Q1} \; + \; g_{P,Q2} q_{Q2}\right] & \end{aligned} \tag{3.16}$$

where $Q1$ and $Q2$ indicate the first and last node on the element evaluated and g represents the coefficients product of the integration of the kernels multiplied by the shape functions; and for the Left-hand side (LHS)

$$\begin{aligned} LHS \rightarrow C(P)\; u(P) + \int_\Gamma q^* \left[N_1 \; N_2\right] \; d\Gamma \quad & \begin{Bmatrix} u_{Q1} \\ u_{Q2} \end{Bmatrix} \\ = C(P)\; u(P) + \left[\hat{h}_{P,Q1} \; \hat{h}_{P,Q2}\right] \quad & \begin{Bmatrix} u_{Q1} \\ u_{Q2} \end{Bmatrix} \\ = C(P)\; u(P) + \left[\hat{h}_{P,Q1} u_{Q1} \; + \; \hat{h}_{P,Q2} u_{Q2}\right] & \end{aligned} \tag{3.17}$$

where $\hat{h}$ represents the coefficients product of the integration of the kernels multiplied by the shape functions. It is convenient to define a new function h identical to $\hat{h}$ only including the factor $C(P)$ to the load point

$$h_{ij} = \begin{cases} \hat{h}_{ij} + C(P) & \text{when } i = j \\ \hat{h}_{ij} + C(P) & \text{when } i \neq j \end{cases} \tag{3.18}$$

where i represents the node on the load point and j represents the node on the field point. Now the entire system of equations can be written in the influence matrix form

$$\mathbf{Hu} = \mathbf{Gq} \tag{3.19}$$

where $\mathbf{H}$ contains all of the h terms resulting from evaluating boundary integrals containing the kernel q^*, $\mathbf{u}$ is a vector containing the known and unknown potentials of the nodes, $\mathbf{G}$ contains all of the g matrix terms resulting from evaluating the boundary integrals containing the u^* kernel, and $\mathbf{q}$ is the vector containing the known and unknown flux densities of the nodes. For the oil zone, where the Poisson equation $\nabla^2 u = S$ applies, the volume integral term in (3.4) becomes

$$\int_\Omega -u * S d\Omega$$

and for the case in which S takes the form of a point source/sink of strength Q at location $\bar{\mathbf{x}}$, this integral term can be rewritten

$$\int_\Omega -u * Q\Delta(\mathbf{x} - \bar{\mathbf{x}}) d\Omega$$

Making use of the integral properties of the Dirac delta function this becomes greatly simplified to

$$-u * (\bar{\mathbf{x}})Q$$

Thus a term, being simply the product of the source pumping strength and the value of the fundamental solution at the pump location, is added to the equation to provide the effect of the pump.

3.2.3 Step 3: Application of Boundary conditions

After obtaining the influence matrix **H**, it is known that a potential u corresponds to every degree of freedom; in a similar way,this occurs with solution matrix **G** and flux densities q. In order to have the system solved, initial values from the boundary become very useful. These initial values are known from the initial boundary conditions in a problem as it was explained in the previous chapter. E.g. if u_1 is known as a Dirichlet BC, it is included in the system, also, if q_2 and q_3 are known from Neumann conditions, they are also to be included as follows:

$$\begin{bmatrix} h_{11} & h_{12} & h_{13} & \cdots & h_{1j} \\ h_{21} & h_{22} & h_{23} & \cdots & h_{2j} \\ h_{31} & h_{32} & h_{33} & \cdots & h_{3j} \\ \vdots & \vdots & \vdots & \ddots & \vdots \\ h_{11} & h_{12} & h_{13} & \cdots & h_{ij} \end{bmatrix} \begin{Bmatrix} \mathbf{4} \\ u_2 \\ u_3 \\ \vdots \\ u_n \end{Bmatrix} = \begin{bmatrix} g_{11} & g_{12} & g_{13} & \cdots & g_{1j} \\ g_{21} & g_{22} & g_{23} & \cdots & g_{2j} \\ g_{31} & g_{32} & g_{33} & \cdots & g_{3j} \\ \vdots & \vdots & \vdots & \ddots & \vdots \\ g_{11} & g_{12} & g_{13} & \cdots & g_{ij} \end{bmatrix} \begin{Bmatrix} q_1 \\ \mathbf{0} \\ \mathbf{0} \\ \vdots \\ q_n \end{Bmatrix} \tag{3.20}$$

3.2.4 Step 4: Solution of the algebraic equations

After including the Boundary conditions in the system (3.19) we are left with known and unknown variables in vectors **u** and **q**. It is appropriate to rearrange the equations to place all of the unknown variables on the LHS and all the known terms on the Right-hand side (RHS) yielding a new algebraic equation

$$\mathbf{Ax} = \mathbf{By} \tag{3.21}$$

where now **A** contains all of the columns of **H** and **G** corresponding to the **x** vector that contains all the unknown variables of the nodes and **B** contains all of the combined functions corresponding to the **y** vector that contains all the known variables of the nodes. This way, the LHS **By** is completely known and can be easily multiplied obtaining vector[1] **z**

$$\mathbf{Ax} = \mathbf{z} \tag{3.22}$$

in this system of equations where both matrix **A** and vector **z** are all known, a standard equation solving routine can be performed to obtain the remaining unknown vector **x**.

3.2.5 Step 5: Calculation of variables at internal points

It is not necessary for this work to calculate any of the values at internal points. However, it is possible to obtain potential of any point inside the solution domain, it can be done very simply after determining all of the unknown potentials and flux densities. All of the boundary values are replaced in equation (3.9) except in this case, the flux density is not normal to the boundary, in any way this can still be differentiated with respect of x or z directions.

3.3 Time stepping and re-meshing

The analysis if of water coning problem simulates the moving interface between the oil and water zones as time advances through the pumping process [13]. It will be treated as a pseudo-static problem [8] in which the Poisson equation is solved (statically) at each time step according to the above steps. At each time step, the change in elevation of any location along the interface can relate to the amount of fluid crossing the interface in some chosen duration, Δt of the time step [2]. This relationship is shown in the expression of equation (2.13), which gives the time in elevation to be made in preparation for the next

[1] Variables **x**, **y** and**z** in bold face are vectors and should not be confused with x, y or z from the Cartesian plane.

time step.

Of course, the change in geometry requires the interface to be re-meshed , but in 2D boundary element implementation this is a simple process.

3.4 Regularisation

Another way to deal with the singularity is to re-write or 'regularise' equation (3.9) with identities developed by Liu et al. [24] using properties of the Dirac- delta function. Resulting in

$$\int_{\Gamma} q^*(P,Q)\left(u(Q)-u(P)\right)d\Gamma(Q) = \int_{\Gamma} u^*(P,Q)q(Q)d\Gamma(Q) \tag{3.23}$$

which is the same as (3.9), except that this is not strongly singular any more. The reason for equation (3.23) is weakly singular is due to the fact that on the LHS of the equation $u(Q)-u(P)$ goes to 0 on the same places where q^* goes to ∞ reducing the order of the singularity. This is the most appropriate form of the BIE for the enriched scheme to be developed and will be the one used on the code used to solve the system.

Chapter 4

Enrichment Approach

The main goal of introducing the idea of enrichment into a finite element or boundary element formulation is to improve its efficiency by reducing the computational resources it needs to produce accurate results, this way new problems in different dimensions can be easily analysed without sacrificing reliability. The combination of the selection of the Boundary Element Method (BEM) over Finite Element Method (FEM) and the enrichment of the method, results in a significant decrease of Degrees of Freedom (DoF) resulting on less evaluations to perform in order to obtain a numerical result. An enriched version of the BEM for potential problems consists in the addition of functions to the original shape functions locally where the effect of a sink acts directly causing a drop in potential and increase in flux density. Preliminary results in the matter have been presented in 2019 [3]; and in this work, tests are conducted to prove the reliability of the problem in different scenarios to be fit for any other initial conditions.

The base of an enrichment scheme has its origins in the Partition of Unity Finite Element Method (PUFEM) presented by Melenk et al. [18] in 1996. In this method, the main feature is the ability to include a previous knowledge about the behaviour of the local system, among other features such as the ability to create finite element spaces of any regularity for the solution of equations of a higher order. In their work, a new method alternative to FEM was presented that allows the user to include functions with good local approximation properties about the problem to be analysed in the finite element space. For this it may be too much to create optimal functions to solve the Partial Differential Equation (PDE); although it is desirable to use the actual mathematical functions known to form the solution either locally or globally, a robust numerical approximation can still be achieved by using functions that only resemble the behaviour of the solution by selecting rough coefficients. According to Melenk et al. [18], this is due to the fact that the special ansatz functions incorporate the rough behaviour of the solution. Examples of local approximation spaces were presented featuring the Laplace's equation, elasticity equations and the Helmholtz equation.

4.1 Methods of enrichment

In engineering practice, physical models include geometries that are not always 'stable' i.e. their shape tend to change when large gradients occur. Typically this happens in time-dependent PDEs where a reconstruction of the mesh for every time step of the analysis is required. These reconstructions in some cases may lead to numerical difficulties. One of the solutions has been the mesh refinement in specific areas of the geometry, where the effect of a source consequences a jump of gradient in said regions. However this idea increases the number of DoF causing an increase of computational effort, opposite to

what is sought. A new approach was presented in 2019 [3], that involved a combination of the original shape functions from the elements most affected by the source and additional equations that capture the behaviour of the unenriched version in a similar problem. This idea emerges from the Partition of Unity Method (PUM).

Other applications have used the enrichment approach as well, and a good example is in fracture mechanics. In the case of Moës et al. [19] in 1999, the work focused on crack growth without re-meshing. Enrichment schemes have their own taxonomy, in which are found problems with crack tips successfully enriched and solved with the extended version of the FEM ie. XFEM. The XFEM, or eXtended Finite Element Method, is charaterised by localised enrichment being used in certain locations of the model that require it, and in a fracture mechanics context this is the (known) local asymptotic fields in the vicinity of crack tips. After the appearance of the PUFEM, applications of approximation functions have been studied, like in wave problems governed by the Helmholtz equation. Lagrouche et al. [25] in 2002 presented new FEM models that were developed based on the partition of unity of isoparametric elements obtaining a more economical model by developing semi-analytical integration schemes. It was shown that accurate solutions could be obtained from coarse meshes when a partition of unity enrichment was used. A partition of unity enrichment can be described as one in which global enrichment functions are used. Laghrouche et al. made use of a plane wave enrichment. This work focused on testing the conditioning of the PUM concluding that PUM discretisation is poorly conditioned regardless of its use, but it is possible to determine 'safe' regions in the $m - k$[1] domain in such way that the conditioning is acceptable and that this framework is acceptable for similar schemes based on higher-order elements in 2D and 3D.

Later in 2004 Perrey-Debain et al., identified a problem of limitations by an upper bound on frequency for the solution of Helmholtz and elastodynamic wave problems with the conventional Finite and Boundary Element Methods for analysis. An overall description of the theoretical background of the BEM's behaviour and ideas from the PUFEM applied to acoustics and a new approach were presented reducing the DoF required per wavelength. Error analysis showed an outstanding performance of the new elements compared to the conventional. Also a significant reduction of the DoF per wavelength was possible going from 8 conventional quadratic elements to only a little over 2 substantially reducing the load of work of the mathematical model.

The design analysis of hybrid numerical-asymptotic Boundary Integral Method (BIM) for the same type of boundary value problems i.e. governed by the Helmholtz equation, that model time harmonic acoustic wave scattering in domains exterior to impenetrable obstacles and its implementation was presented by Chandler-Wilde et al. [26]. Here a combination of conventional polynomial approximation and high frequency asymptotic lead to basis functions suitable for the representation of the oscillatory solutions. In their experiments, they concluded that hybrid methods are effective computational algorithms even though the error cannot be fully analysed. In this work certain assumptions are made that preclude the use of the method to simulate cases in which there are multiple reflections between different obstacles or within the same non-convex obstacle.

The latest study suggests a new approach based in BEM and partition of unity BEM for the solution of shortwave problems governed by the Helmholtz equation. The work was presented by Gilvey et al. [27] in 2019 which presented an enrichment approach to solve efficient and accurately wave-scattering problems by polygonal obstacles with the Helmholtz equation. The methods employed for numerical testing include the BEM and Partition of Unity boundary element method (PUBEM). In their work they propose a modification in the shape functions of the element enriched. These enriched elements, for this case are in the vicinity of a sharp corner. The enrichment functions are taken from the leading order

[1]Domain in which m is the number of plane waves and k wave number for Laghrouche's [25] analysis.

term in the series of fractional-order Bessel functions that are known to form the singular solution space in wave scattering by sharp corners. It is possible that this approach may also work in the potential problem's scheme, where the traditional shape functions are enriched to reproduce a behaviour. With enriched elements, it would be possible to significantly drop the DoF and still obtain reliable results.

4.1.1 Enrichment in potential problems

O'Hara et al. [28] presented in 2009 a work that consisted in the analysis of potential problems that presented sharp thermal gradients in heat transfer. In 2011 an update on the same project [29] was presented, only this time using coarse finite element methods obtaining excellent results in the implementation of their experiments. Based on the good results obtained, Diwan et al. [30] in 2014 analysed two different applications (a) wave scattering and (b) heat transfer. In both cases, Diwan et al. reduced the number of DoF without sacrificing accuracy. The work by O'Hara et al. yielded good results that lead to further research on enrichment for potential problems.

These methods of enrichment have roots in analytical solutions of the problem to be enriched, however, another approach has been presented for the enrichment and solution of problems where an analytical solution is not possible to calculate. In this case, the enrichment resembles or approximates the behaviour of a reference solution from the unenriched version of a similar problem [17]. Within this reasoning, in a two zone potential problem new options are available to explore. The idea of using an approximate enrichment function, based on engineering experience of similar problems, was presented by Mohamed [17] for problems of heat transfer time-dependent heat transfer. Motivated by the fact that experience suggests the temperature distributions around heat sources to resemble Gaussian distributions, enrichment functions of this type were used in a PUFEM simulation, and results of high accuracy obtained from coarse meshes. In the current thesis, this idea is explored for the enrichment of the flux density over the interface in the water coning problem.

4.2 Choice of enrichment

The work presented by the current author in [3] in 2019 is based upon enrichment ideas from previous research, with ideas from Mohamed [30]. Enrichment in a moving-boundary potential problem governed by the Laplace equation is achieved obtaining good results. In the previous chapter, the regularised form of the Boundary Integral Equation (BIE) (3.23) had been established. Here u^*, q^* are the fundamental solutions for the Laplace operator in 2D and S describes the strength of a sink in the domain Ω. In forming a BEM solution scheme based on (3.23), researchers typically employ a classical polynomial approach where a classical discretisation involves the expansion of u and q in low order polynomial shape functions N_j, over each element containing J nodes and parameterised by local coordinate $\xi \in [-1, 1]$ in the usual way

$$\begin{aligned} u(\xi) &= \sum_{j=1}^{J} N_j(\xi) u_j \\ q(\xi) &= \sum_{j=1}^{J} N_j(\xi) q_j \end{aligned} \tag{4.1}$$

The enrichment scheme chosen consists on adding a set of enrichment functions. As mentioned before, these will enable the element to enhance the behaviour of the unenriched model

$$u(\xi) = \sum_{j=1}^{J} N_j(\xi) u_j + \sum_{m=1}^{M_u} \lambda_m^u \psi_m^u(x) \tag{4.2}$$

$$q(\xi) = \sum_{j=1}^{J} N_j(\xi) q_j + \sum_{m=1}^{M_q} \lambda_m^q \psi_m^q(x) \tag{4.3}$$

where ψ_m^u and ψ_m^q are sets of enrichment functions designed to efficiently capture the variation in the potential u and flux density q respectively and the terms λ_m^u and λ_m^q are the amplitudes of these enrichment functions, and will be found as part of the solution vector alongside the more traditional unknowns in a boundary element simulation. It should be noted that over the elements enriched in this way, the unknowns u_j and q_j can no longer be understood as nodes of u and q; thus, the number of degrees of freedom has to increase by introducing M_u and M_q in such way that the same number of additional equations need to be performed in order to retain a square system. These may be found from the consideration of 'additional collocation points' at non-nodal locations (in this case 3, one for potential and one for flux density). Though in conference paper [3] by the current author one more additional collocation point was included as an 'oversample' so that additional equations yield more information than the minimum (3 in this case), leading to an overdetermined system of equations that needs to be solved in a least squares sense. There is considerable freedom in placement of the additional collocation points; they can be placed anywhere on the boundary or interface with the exception of the nodes. Different locations were investigated, as described in Section 4.4, and the best solution was found to be to place them on the interface evenly spaced between the nodes. As an illustration of how this can be implemented in a BEM setting, the traditional left hand side **Hu** and right hand side **Gq** for a problem enriched using $M_u = 1$ and $M_q = 2$ become:

$$\mathbf{Hu} = \begin{bmatrix} h_{1,1} & h_{1,2} & h_{1,3} & \cdots & h_{1,22} & h_{1,23} \\ h_{2,1} & h_{2,2} & h_{2,3} & \cdots & h_{2,22} & h_{2,23} \\ h_{3,1} & h_{3,2} & h_{3,3} & \cdots & h_{3,22} & h_{3,23} \\ \vdots & \vdots & \vdots & \ddots & \vdots & \vdots \\ h_{24,1} & h_{24,2} & h_{24,3} & \cdots & h_{24,22} & h_{24,23} \\ h_{25,1} & h_{25,2} & h_{25,3} & \cdots & h_{25,22} & h_{25,23} \\ h_{26,1} & h_{26,2} & h_{26,3} & \cdots & h_{26,22} & h_{26,23} \end{bmatrix} \begin{Bmatrix} u_1 \\ u_2 \\ u_3 \\ \vdots \\ u_{22} \\ \lambda^u \end{Bmatrix} \tag{4.4}$$

and

$$\mathbf{Gq} = \begin{bmatrix} g_{1,1} & g_{1,2} & g_{1,3} & \cdots & g_{1,44} & g_{1,45} & g_{1,46} \\ g_{2,1} & g_{2,2} & g_{2,3} & \cdots & g_{2,44} & g_{2,45} & g_{2,46} \\ g_{3,1} & g_{3,2} & g_{3,3} & \cdots & g_{3,44} & g_{3,45} & g_{3,46} \\ \vdots & \vdots & \vdots & \ddots & \vdots & \vdots & \vdots \\ g_{24,1} & g_{24,2} & g_{24,3} & \cdots & g_{24,44} & g_{24,45} & g_{24,46} \\ g_{25,1} & g_{25,2} & g_{25,3} & \cdots & g_{25,44} & g_{25,45} & g_{25,46} \\ g_{26,1} & g_{26,2} & g_{26,3} & \cdots & g_{26,44} & g_{26,45} & g_{26,46} \end{bmatrix} \begin{Bmatrix} q_1 \\ q_2 \\ q_3 \\ \vdots \\ q_{44} \\ \lambda_1^q \\ \lambda_2^q \end{Bmatrix} \tag{4.5}$$

The distribution of the flux density resembles a 'cusp' and is found to be well approximated by a Gaussian distribution; in the case of the potential distribution, this is found to be well approximated by a second order rational function [3]. Since conventional linear boundary element models can provide good approximations of the potentials for this problem, we proceed with a low level of potential enrichment, taking $M_u = 1$.

The set of enrichment functions are chosen given the nature of the problem, which is governed by the Laplace equation but also includes a time-dependent iteration scheme. The schemes have proven to work with other type of problems ie. crack tips and shortwave problems; but none have been performed in a

two-zone moving interface problem. This set of enrichment functions will only be applied to the localised elements where sharp piezometric gradients are found. These gradients are found in the interface, where no boundary conditions are applied and the effect of the sink affects directly. The problem has been discretised in the past by [2] where 50 elements were used in this interface for the same reason. With the proposed enrichment scheme, only 4 elements will be defined on the interface, meaning a reduction of 92% of the elements compared to [2]. Only the two central elements from the interface will be enriched to reproduce the behaviour of the solution.

4.3 Performance indicators

Indicators are always required as a point of reference to guide any improvement process, for this reason, two main metrics are used as indicators to determine the accuracy and reliability of any modifications to the code on the different strategies proposed. A useful metric has to be implemented as a point of reference to explore different parameters. Firstly the 'Total flux' Q_Γ is an indicator employed to explore new and different parameters on the same problem. To obtain the total flux, a numerical integration is performed calculating the area under the flux density curve on the interface

$$Q_\Gamma = \int_{\Gamma_{ow}} q \, d\Gamma \tag{4.6}$$

where q is the flux density along the interface Γ_{ow}. Although the total flux provides a useful guide to the numerical accuracy of a scheme, it is rather simplistic and on occasions has been found by the author to fail as an error indicator, since by the cancellation of positive and negative errors a poor solution can be incorrectly reported as good. An improved error indicator is also used, which is not susceptible to the shortcomings of the total flux approach. This is based on a relative L^2 error norm or the 'euclidean' norm, and it is implemented as follows

$$\epsilon_{L^2} = \frac{\left\| q - q^{ref} \right\|_{L^2(\Gamma_{ow})}}{\left\| q^{ref} \right\|_{L^2(\Gamma_{ow})}} \tag{4.7}$$

where q represents the flux density of the model to be evaluated and q^{ref} represents the flux density of the reference model being the results of a refined polynomial BEM model. It should be noted that for this particular problem, an analytical solution cannot be obtained as a reference solution, however, as the refinement of the unenriched BEM increased, the variation of the result on each refinement resulted smaller reaching a point where this variation became trivial as shown in Figure 4.1. Assuming a refinement of 600 elements on the interface, q^{ref} is generated as this is considered the closest to a possible analytical solution.

Other metrics are also useful as a guide for the author as it is the case of the Height of the middle point of the interface (in level to the pumping sink) which aids to notice whether the fluids reach a point where they would mix. Another case is the Flux of the middle point of the interface which reveals how much liquid goes into the pump per unit of time and serves as an index to which scenario works best.

4.4 Tests presented

This work included consideration of seven strategies for different purposes. The first set of tests undertaken look for better ways of forming the numerical method 1) inclusion of additional collocation points over the interface; 2) development of optimised enrichment functions for the flux density; 3) study of different number of Gauss Points for numerical integration. The second part consists on making changes

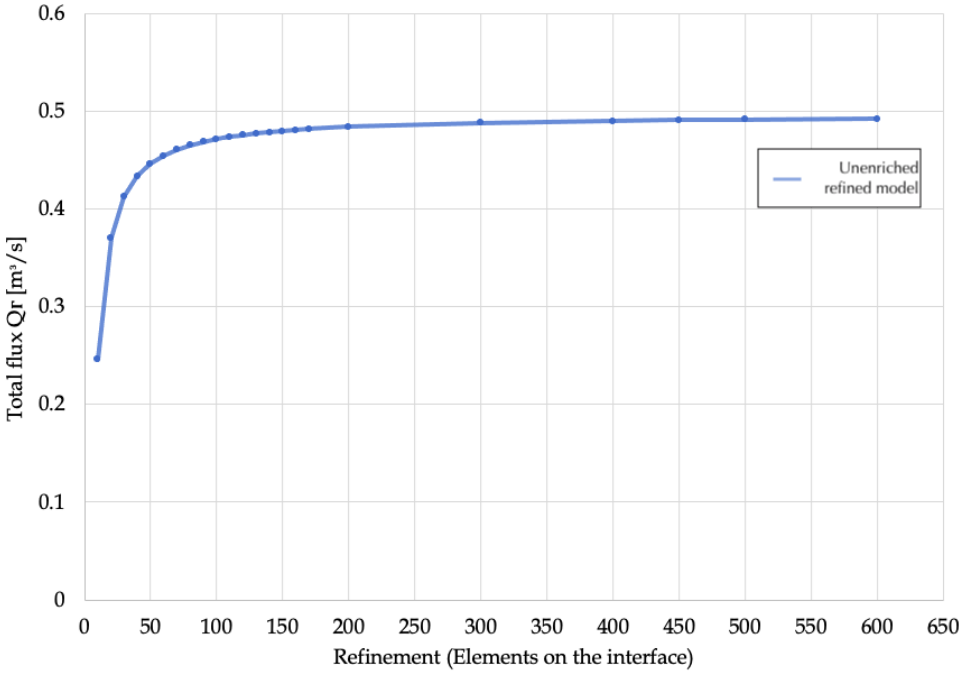

Figure 4.1: Total flux variation in the Unenriched BEM refined model

to the different parameters or conditions of the actual problem to make sure that the enrichment scheme continues performing correctly, 4) different problem conditions such as strength and position of the sink; 5) stopping at different time steps to observe the behaviour ; 6) change the density of the liquids; 7) change the shape of the geometry and an extra test 8) that integrates all the strategies that have shown a good result combined.

In the work presented in 2019 [3], the present author proposed the idea of increasing the number of collocation points along the interface, this might be expected to have a better solution because increasing the number of collocation points increases the number of equations in the BEM settings (4.4) and (4.5) without the need of increasing the number of elements in it. This way an 'oversample' occurs having more equations than unknowns expecting a better result if the number of collocation points is increased as suggested in [31]. Additional collocation points will yield more information about the coordinates where they are located, and this location may be chosen by the author. For this reason two approaches are tested; a) the first is to add additional collocation points evenly through the outer boundary without subtracting the collocation points already included at the interface as seen in Figure 4.2, b) the second

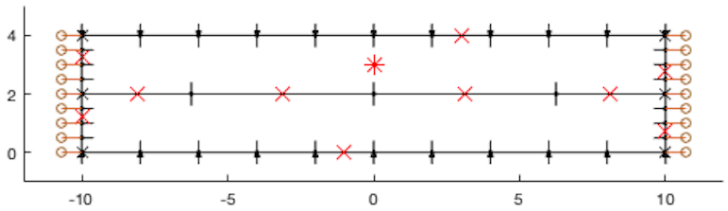

Figure 4.2: Additional collocation points strategy on boundary

approach is to only try collocation points along the interface. The strategies are illustrated a through f

in Figure 4.3. The distribution on these strategies varies in both number and position of the Additional Collocation Points (ACPs).

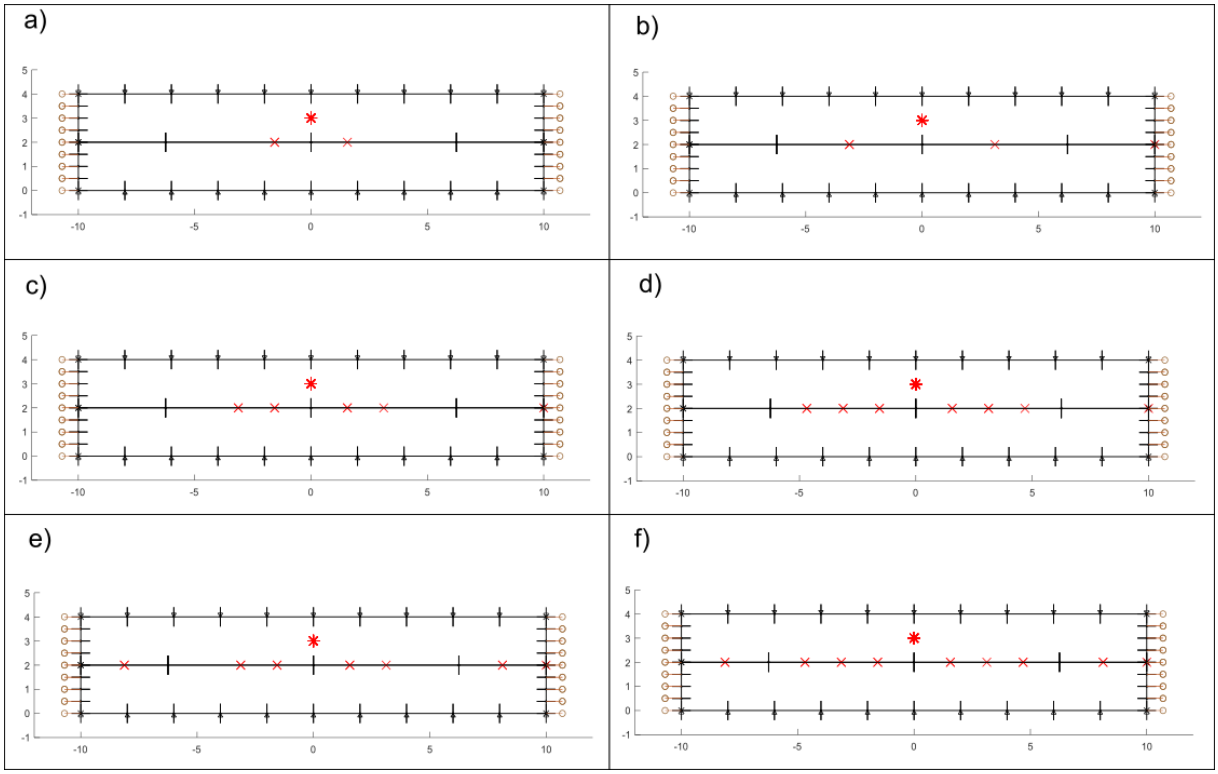

Figure 4.3: Additional collocation points strategies on interface

In this same work presented by the current author [3], an enriched scheme was developed by Chen where the shape functions for the flux density ψ^q were designed to fit the unenriched model presented by Gontijo [2]. The results presented were considered to be 'preliminary' because the enrichment functions were created in order to be optimal for one particular problem. The proposed strategies' goal is to make them suitable for the problem with different parameters ie. different fluid densities, different geometry, or different pump heights. Gontijo describes the behaviour of the flux density along the interface with a graph that resembles the behaviour of a Gaussian. The current author found the flux density to be well approximated by the sum of two Gaussian distributions. A combination of functions were designed combining two Gaussian functions through a sum applying the least square fit method. In this method, the exponential curve is fitted according to the distribution yielding the sum

$$\psi^q = \mathbf{e}^{-(x/s_1)^2} + \mathbf{e}^{-(x/s_2)^2} \tag{4.8}$$

where x is the horizontal point in the plane evaluated with $x = 0$ describing the location of the sink and s_1 and s_2 are independent variables that describe the sharpness of the peak in the distribution. A way to simplify the approach, is to convert this into a single exponential equation, with only one function instead of a sum of two. As a result, the shape of the graph can still be adjusted with the variable s

$$\psi^q = \mathbf{e}^{-(x/s)^2} \tag{4.9}$$

making it broad or narrow but different from equation (4.8) this time the adjustment can be made in the whole distribution, not only the top or bottom of it. This approach is later modified to resemble better the original distribution by modifying the exponent of the Gaussian. Originally squared, it is found that giving a variable exponent, this will allow the enrichment function to be designed with more flexibility to approximate the required flux density distribution. The result of the modified version for this will be

$$\psi^q = \mathbf{e}^{-(x/s_1)^{s_2}} \tag{4.10}$$

where the exponent 2 from (4.9) has been changed to a constant that may be optimised.
The model employed by Gontijo [2] consisted on a refined mesh of 50 elements on the interface, this refinement is used as a reference point to evaluate the numerical performance of the enriched schemes with the performance indicators described.
Several options for s_1 and s_2 values explored in order to determine optimal values of s_1 and s_2. This combination is chosen through a response surface where the minimum value of ϵ_{L^2} is presented.

As this project is based on numerical simulation an integration method had to be selected to evaluate the regularised form of the BIE (3.23). In this case the employed method adheres to the work on [3] employing the Gauss-Legendre quadrature and in an initial implementation 10 Gauss points per element are used. One way to reduce computational effort can be to decrease the number of Gauss points that the numerical integration uses, but this also may sacrifice accuracy of the model. The idea of conducting a study of the number of Gauss points within a range of 6 to 80 per element is implemented, in order to analyse the cost-effectiveness of higher order integration.

It is noted that the process for determining the enrichment functions involves fitting of exponential functions to refined (unenriched) BEM simulations of the problem as proposed. It is therefore to be expected that the solutions of an enriched scheme for the same problem would be very accurate. A more appropriate test of the formulation would be to use these enrichment functions to study a different problem. For this reason the enriched BEM formulation is tested on a range of models having different pump locations (Figure 4.4) and having a different analysis domain geometry (Figure 4.5). where the pumping sink is located in a) coordinates (0,3.5) in the $x-z$ plane ie. 1.5 metres above the interface; b) coordinates (0,3) in the $x-z$ plane ie. 1 metres above the interface; and c) coordinates (0,2.5) in the $x-z$ plane ie. 0.5 metres above the interface.

Another interesting subject of study is the behaviour of the model on different time steps passed after the pump becomes active at different pump heights as this can help clarify how ϵ_{L^2} behaves for the proposed heights of the pump. For this part of the simulation, the pump is stopped at different moments after it is active. The number of tested time steps are 5, 10, 19, 20. Note that every time step has a time span of 2.67 seconds.

A way to prove that the model works very well is to try another 'random' geometry as a 'real' oil reservoir would look like. To do this, the boundaries are modified and the model is tested again with the conditions from previous tests that have worked, in this case the height of one of the sides is modified, also, the top and bottom boundary of the model are modified by including a cosine function to produce waves from side to side as it is presented in Figure 4.5. The interface will remain horizontal as it still the natural initial state resulting from the fluids having different densities.

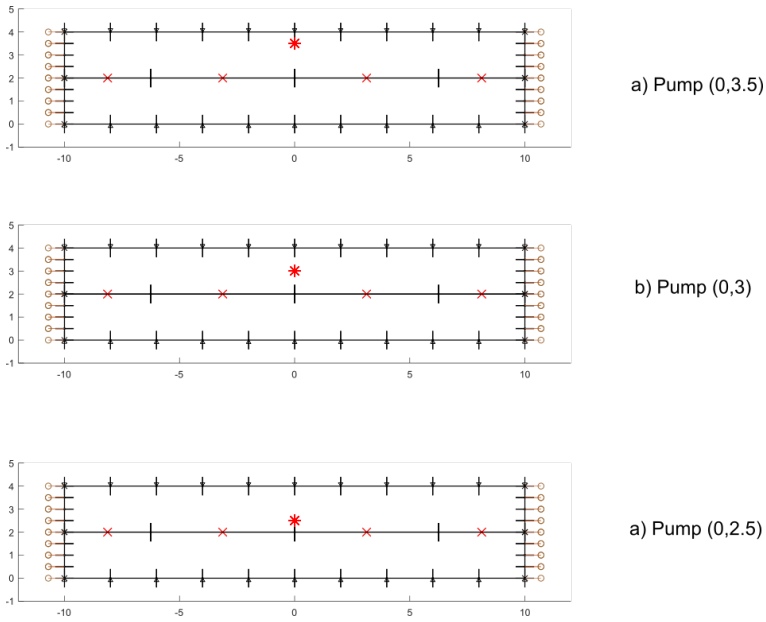

Figure 4.4: Geometry with different heights of the pumping sink

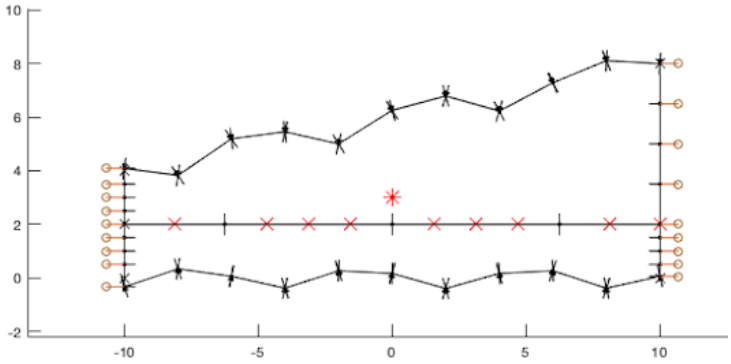

Figure 4.5: Proposed different geometry of the problem

Notice that the number of elements is not modified in this test.
Finally all the strategies with results concluded to be successful will be arranged to work together to see a final composed simulation.

Chapter 5

Results and discussion

In this chapter, the results from the different tests are presented with a discussion on the behaviour of the model. Every approach tested is presented individually except for the final result which incorporates all the optimised strategies.

The first enrichment approach applied to this problem, presented in 2019 [3] suggests discretising the interface in 4 elements rather than 50. This was done by enriching the middle elements on the interface (closest to the pumping sink) with equation

$$\psi^q = \mathbf{e}^{-(x/0.6429)^2} + \mathbf{e}^{-(x/2.1114)^2} \tag{5.1}$$

from (4.8). The values $(s_1, s_2) = (0.6429, 2.1114)$ were found using a least squares fit to the flux density distribution over the interface, this was generated using a refined polynomial Boundary Element Method (BEM) formulation with 50 elements on the interface, taking into account all time steps in the simulation for the test problem described in section 4.4. The analysis using four elements, along with

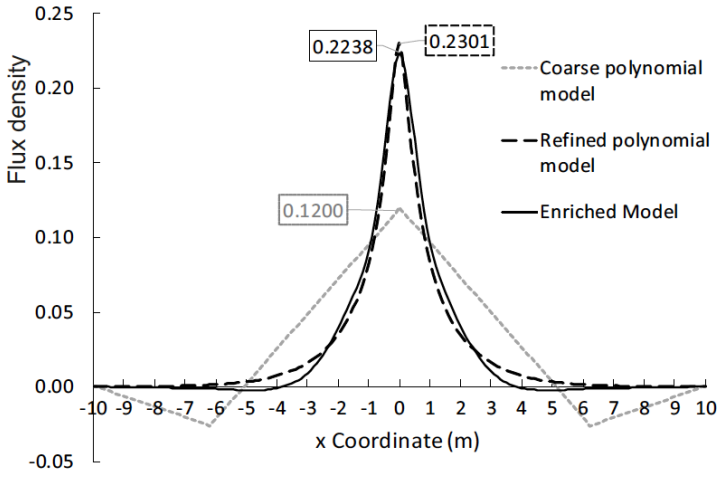

Figure 5.1: Original interface flux density distribution

the enrichment function (5.1), is seen to perform well. Figure 5.1 (reproduced from conference paper [3]) shows the flux density distribution from the reference (refined polynomial BEM) solution to be well approximated by the enriched BEM scheme. Also shown, for completeness, is the result from a discretisation of four elements on the interface (i.e. the same discretisation as the enriched scheme) but without

enrichment. As can be expected, this coarse mesh of linear elements is incapable of accurate predictions. Notice that s_1 and s_2 have been replaced by the fitted values that most resemble the unenriched model as shown in Figure 5.1 from [3]. This flux distribution was obtained with the combined enrichment equation (5.1) for flux density. The analyses geometry were set as described on Section 2.3 having 20 metres separation between the vertical boundaries and 4 metres separation between top and bottom boundaries. The interface is assumed to be in the middle of both top and bottom boundaries yielding zone 1 at the bottom and zone 2 at the top; the location of the pumping sink is in the middle of this last one with assumed coordinates of (0,3) in the $x-z$ plane. Recalling, from Section 1.4, that the focus of the current research is only the enrichment of the potential flow approximation to the full water coning simulation, a simple approach is adopted in which a) the densities of the two zones are equal, being $\rho_1 = \rho_2 = 1000[^{kg}/_{m^3}]$; b) the gravitational acceleration g is of 9.81 $[^{m}/_{s^2}]$; c) absolute permeability k of 1 [darcy]; d) porosity of medium θ of 1; and e) dynamic viscosity for both zones $\mu_{1,2}$ of 0.001. These conditions were programmed to simulate the process with a e) constant pumping rate of $-1.5 \times 10^{-3}[^{m^3}/_{s}]$ f) stopped after 20 time steps with a time span of $2.67[s]$ per time step for analysis purposes. As stated on the previous chapter, in Section 4.4 the integrals in the numerical simulation are evaluated with the Gauss-Legendre quadrature with g) 10 Gauss Points. With a collocation point strategy of four collocation points as presented in Section 4.4.

One of the most tangible forms of evidence demonstrating the success of an enriched BEM formulation is the convergence in the Total flux along the interface between both zones Q_Γ. Since no analytical solution is available, the convergence is presented in Figure 5.2 in the form of a plot where the Total flux

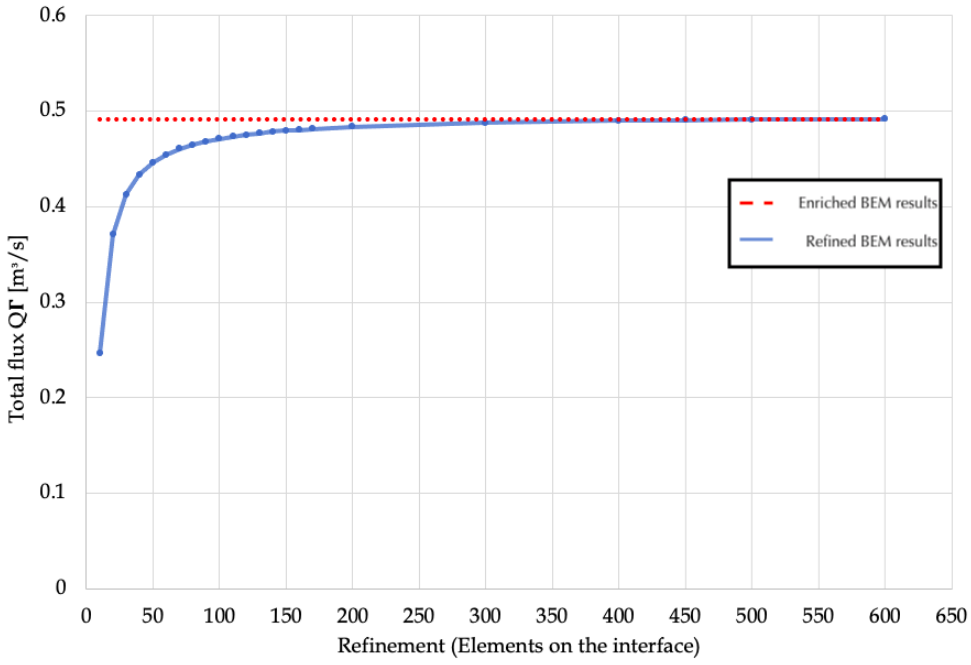

Figure 5.2: Convergence of the unenriched model

across the interface Q_Γ (y-axis) evaluated at time step 20 behaves against scenarios where the number of elements on the interface becomes greater (x-axis). The red dots show the enriched BEM result using only 4 elements on the interface, and it is clear based on the behaviour of the unenriched model (Figure 5.2 Blue line) that without enrichment it would take a mesh of several hundred elements on the line to reproduce the accuracy of the enriched model. As the refinement of the un-enriched model increased, the

simulation would yield a closer result to the the most accurate solution. Notice that the plot reaches a point where the results are so close together that the error becomes negligible. This is why it is acceptable to use this point as a reference solution to calculate the error of the L^2 norm ϵ_{L^2} further in this study. This analysis proves that it is possible to simulate the problem efficiently using an enriched BEM formulation and, high accuracy can be achieved. It should be noted that this high accuracy is found when the enrichment functions are optimal in the sense that they were derived by fitting data to results of a previous unenriched simulation *of the same problem*. For this reason we would expect to recover an accurate solution using the enrichment functions generated in this way. From a scientific point of view, it is known that both the unenriched and enriched methods are approximations and come with an error. The following sections describe some numerical experiments designed to improve the enriched formulation; error analyses are also performed to draw conclusions about how an enriched scheme may be optimised.

5.1 Additional Collocation Points

The first set of tests that were performed include Additional Collocation Points (ACPs) on the boundary in addition those required on the interface as discussed in Section 4.4. The code is executed with function (5.1) as a standard for all tests and the conditions described in the beginning of the current chapter where the pump stops at time step 20, unless otherwise specified. The results of each strategy are presented

Strategy	$\mathbf{Q_\Gamma}$ $[m^3/s]$	$\boldsymbol{\epsilon_{L^2}}$	**Flux density** $[m^3/s]$	**Maximum height** $[m]$
Interface only	0.4913	4.3107%	0.2238	2.2674
Interface + boundary	0.4913	4.157%	0.223	2.2664
a	1.3749	266.5821%	0.6761	2.5916
b	1.4088	287.3923%	0.699	2.6161
c	0.4914	4.8551%	0.2267	2.2785
d	0.4915	4.5807%	0.2253	2.2716
e	0.4916	4.8453%	0.2267	2.2788
f	0.4919	4.5307%	0.2251	2.2699

Table 5.1: Results from Additional Collocation Points' strategy

in Table 5.1 and consist of four main results that include the Total flux on the boundary Q_Γ, Error of the L^2 norm ϵ_{L^2}, maximum value of the flux density located at the mid-point of the interface, and finally Height of the interface that is also located in the mid-point of the interface. These metrics were discussed in Section 4.3 and are chosen to help compare the improvement of each strategy from different perspectives. When the ACP strategy is implemented, the author has to take into consideration that the number of ACPs has to be superior to the number of additional equations from the solution matrix. The first two tests from this strategy (a) and (b) do not follow the previous statement on purpose and prove that this statement is correct as both results show an error ϵ_{L^2} over 200%, for this reason these results are omitted on further analyses as well as in Figure 5.3. This approach was executed with the only purpose of obtaining a result and understanding behaviour of the result. In Table 5.1 the 'Strategy' column represents the approach that has been tested as proposed by Figure 4.3. This would reveal whether the increment of collocation points improves the Total flux Q_Γ that has been measured so far. It must be taken into account that the improvement is good but yet trivial and this method would increase the computational effort if the addition of these points continues. Figure 5.3 indicates the relationship between the approach from the strategies on the x-axis against the Total flux $Q_\Gamma[m^3/s]$ on the y-axis where the increment is well appreciated in regards to the increment of collocation points represented on

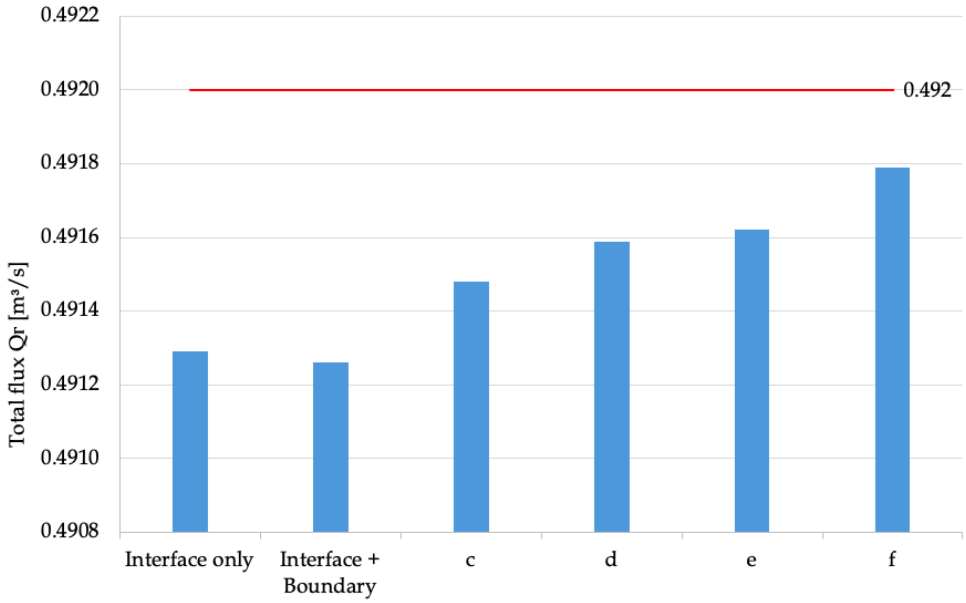

Figure 5.3: Total flux results from Additional Collocation Points' strategy

the blue bars; it can also be observed how close it gets to the reference solution represented with a red line. These analyses arise questions on how the changes may affect other aspects such as the relative error of the L^2 norm ϵ_{L^2} so more tests are considered. In Figure 5.4 a sacrifice on accuracy is demonstrated as

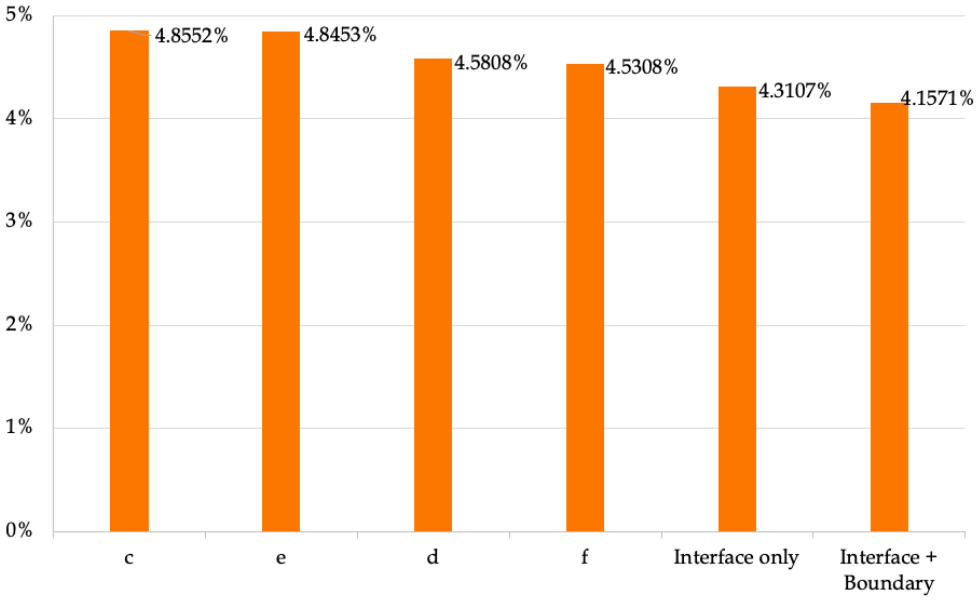

Figure 5.4: Error results from Additional Collocation Points' strategy

the relative error increases; however, this increment is only different by no more than 0.8% as shown in the data from Table 5.1. Notice that in the same figure, the orange bars are sorted by error ϵ_{L^2} from the largest to the smallest, this allows to appreciate that the error in this case is acceptable in engineering terms. A relationship analysis is implemented to determine which strategy works best as the behaviour of both indicators is not the same. Figure 5.5 represents this relationship where the x-axis presents the amount of accuracy that this represents whereas the y-axis represents the Total flux Q_Γ that is obtained

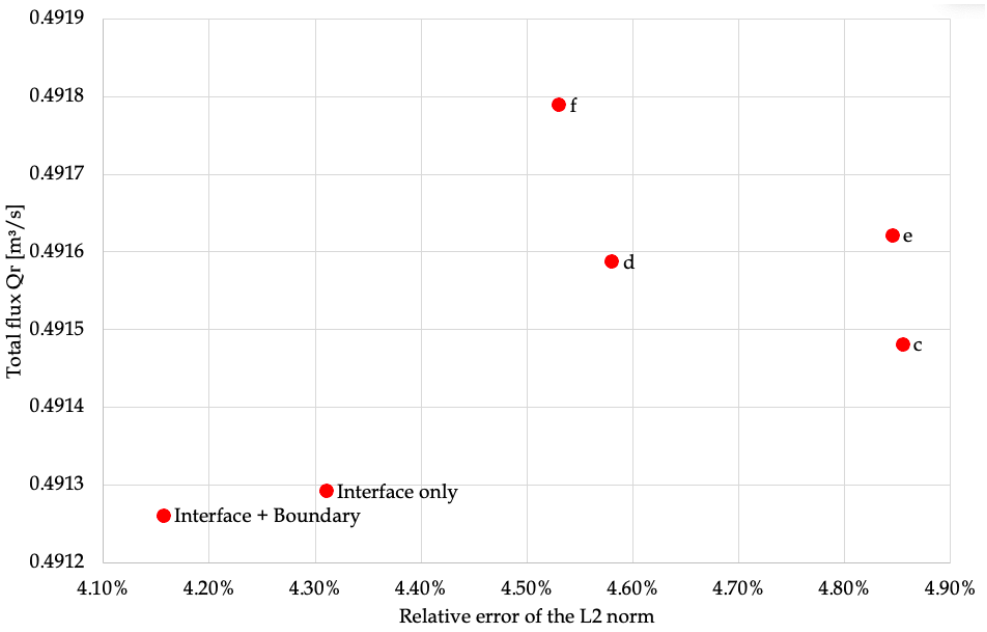

Figure 5.5: Correlated results from Additional Collocation Points' strategy

from the simulation. This way, the best option can be determined as the one that provides the most Total flux Q_Γ value with the least error possible ϵ_{L^2}, in this case strategy 'f'. It is reasonable to trust this plot as it can be observed that strategies 'd' and e' coincide to have better values for Total flux Q_Γ with the same number of ACP; however strategy 'd' yields more accuracy. In a similar way, strategies 'c' and 'e' have similar error as the number of ACP on the mid-point of the geometry is lower. The author also observes that a cost of error and computational effort is occurs for every increment on ACP, for this the tests on this matter cease.

5.2 Changes to the enriched shape function

It has been defined in the previous chapter that a function ψ^q is required for the successful enrichment of the selected elements. As stated before, this function has been fixed yielding a combined Gaussian function that, as expected, delivers results of high accuracy from a very coarse discretisation. The challenge now is to simplify the flux density enrichment function in a way that good results are obtained with different conditions on different problem geometries exhibiting different pumping conditions.

5.2.1 Single Gaussian Equation

Enrichment function ψ^q is simplified as shown in (4.9) having only one exponential equation. This leaves only one variable s which is now modified to find the best value to resemble the flux density's distribution of the model. Based on the results from [3] where $s_1 = 0.64$ and $s_2 = 2.11$ the model with (4.9) is tested with a range of possible values for s in the range $s \in [1/5, 3]$ remembering that the higher the value given to s, the broader the distribution. This simulation runs with the new proposed enrichment function (4.9) and under the same conditions as presented at the beginning of the chapter, densities, gravitational acceleration, absolute permeability, porosity of the medium, dynamic viscosity, pumping rate, and time span and Gauss points to maintain the proposed standard in this research. The results of these analyses are shown in Table 5.2 containing a) Total flux Q_Γ, b) Error of the L^2 norm ϵ_L^2, c) Flux density and d) Maximum height of the interface (tip of the curve to monitor that the water does not reach the pump and compromise the oil extraction). The results show a large error on the smallest s values and drops

s	Q_Γ $[m^3/s]$	ϵ_{L^2}	**Flux density** $[m^3/s]$	**Maximum height** $[m]$
1/5	0.4311	4.2114	0.8311	2.7362
1/4	0.4769	3.0258	0.7122	2.6641
1/3	0.4915	1.4829	0.5287	2.536
1/2	0.4861	0.4265	0.3584	2.396
0.64	0.4850	0.1796	0.297	2.3396
2/3	0.4849	0.163	0.2888	2.3318
3/4	0.4852	0.1326	0.2677	2.3115
1	0.4885	0.095	0.2272	2.271
3/2	0.4930	0.1302	0.187	2.2289
2	0.4958	0.1923	0.167	2.2072
2.11	0.4965	0.2053	0.1636	2.2035
5/2	0.4990	0.2542	0.1521	2.1907
3	0.5025	0.345	0.1335	2.1694

Table 5.2: Results from Single Gaussian analysis sorted by "s"

dramatically as the value approaches one of the original s values 0.64. These results are plotted for better appreciation of the flux, error of the L^2 norm and height of the interface.

Firstly, Figure 5.6 is produced and analysed with focus on the behaviour of the Total flux Q_Γ as s is

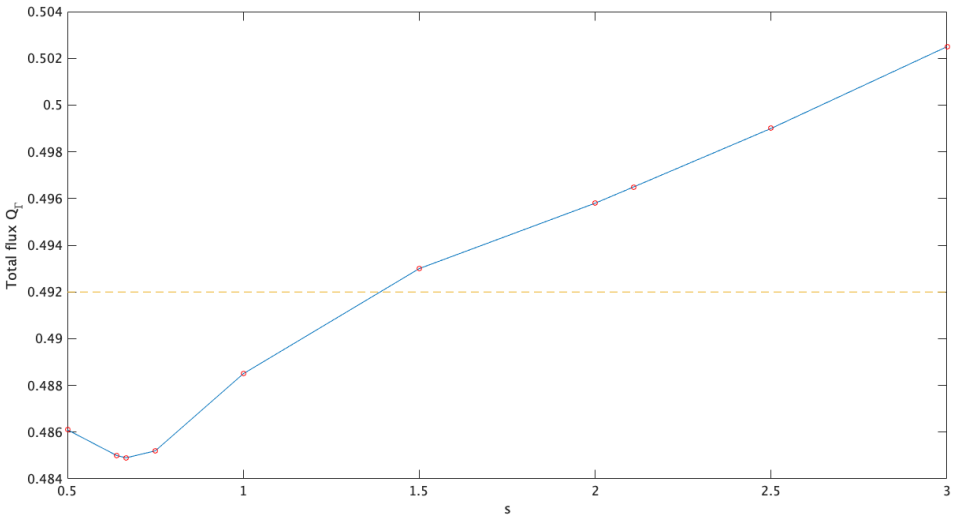

Figure 5.6: Analysis of Q_Γ on different s

modified. The values for Q_Γ indicate a good flux value specially where where $s > 2$. Notice that the dotted line in amber colour represents the reference limit from the refined polynomial $Q_{ref} = 0.492[m^3/s]$. This plot also confirms the hypothesis that the cases with a lower s have broad Gaussian distribution and will be unable to resolve the sharpness of the peak that develops in the in the flux density distribution, particularly in the later time steps. It should be noted that any results for this analysis where $s > 1/2$ are invalidated as it can be observed in Table 5.2 that the Height of the interface compromises the extraction of the hydrocarbon.

Secondly, to cross analyse the results from the previous plot, Figure 5.7 is produced which represents the behaviour of the error of the L^2 norm on different s values. With this new plot the behaviour of the error

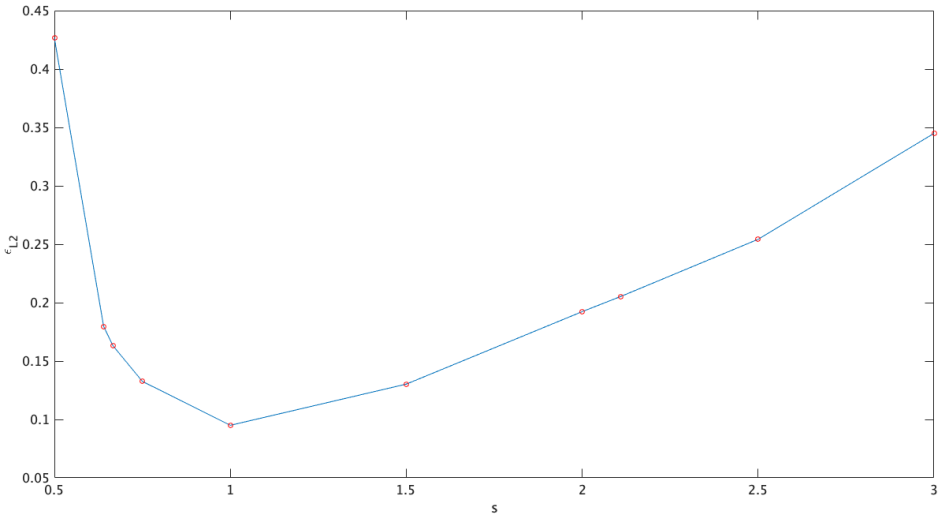

Figure 5.7: Analysis of ϵ_{L^2} on different s

of the L^2 norm the author can easily determine that the best s value is between ½ and ⅔. Notice that in this case any results for this analysis where $s > 1/2$ are invalidated as well based on the results presented in Table 5.2, where it can be observed that the Height of the interface compromises the extraction and the BEM solution is invalid since the assumption that the pump lies in the upper zone becomes violated. As for the flux density, it is enough to observe from Table 5.2 that it is better as s becomes lower.
The intention of this set of simulations is to find the best alternative for a new function that captures the essence of the shape of the flux density plot from the unenriched BEM without having to include a combined Gaussian function or combined exponent function like (4.8). At the end of this section, a comparison between the best s values according to Figure 5.6 is presented to clarify the reason of the growth of error observed in Figure 5.7.

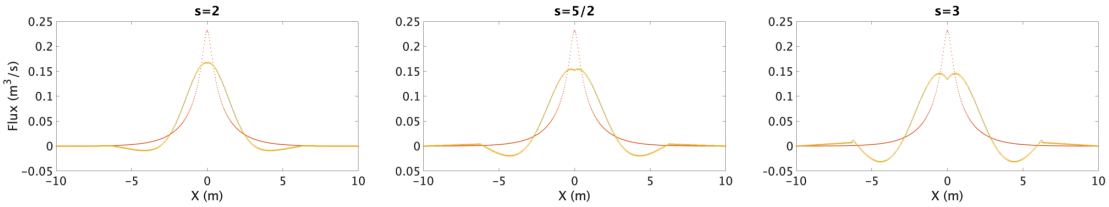

Figure 5.8: Flux density distribution where $s = 2, 5/2, 3$

5.2.2 Single Exponential Equation

First modification to enrichment function

So far the simulations presented have been of a single exponential as written in (4.9) with a single possible variable s. It is now time to test (4.10); in order to do so, only two values for the second s or s_2 are selected to observe the behaviour of the error. The chosen s_2 values for these tests are not chosen arbitrarily; $s_2 = 2$ is selected because this value showed the best total flux as observed in Figure 5.6 that also resembled the reference solution as observed in 5.8; in a similar way $s_2 = 1.2$ is selected because this value showed to have the least error of the L^2 norm in Figure 5.7. This simulation also runs within a range $s \in [1/5, 3]$ In Figure 5.9, the orange line represents the behaviour of the error of the L^2 norm ϵ_{L^2}

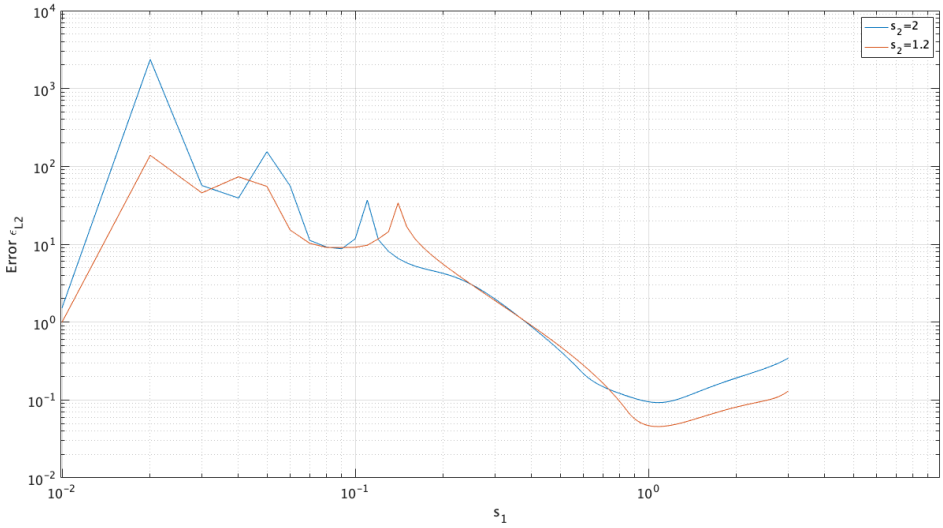

Figure 5.9: Analysis of ϵ_{L^2} with different s_2

where $s_2 = 1.2$ and the blue line represents the same behaviour where $s_2 = 2$. It can also be observed that in both cases the error is minimised around $s_1 = 1$ and conversely, the error becomes unacceptably large for values of $s_1 < 1/2$, similar to the behaviour of Figure 5.7.

Second modification to enrichment function

As good results are obtained replacing the double exponential function (4.8) with the single exponential function (4.9), more questioning for improvement arises and the fixed exponent from (4.9) is tested with a range of values instead of only two, the same way that s_1 has been tested in order to find the best combination of numbers that yield the most accurate s_1 and s_2 values using the new enrichment function (4.10). Response surface methods are a useful approach in optimising in a wide variety of engineering and scientific problems containing multiple input variables. By sampling the results of numerous combinations of the input variables, and plotting the resulting output quantity, a surface is formed showing the performance over the design space. Where there are two input variables (as in the current analysis, s_1, s_2) a surface may be visualised in a 3D plot. For more input variables the response surface becomes a hyper-surface in a multidimensional space that cannot be visualised, but can still be analysed mathematically. Depending on the regularity of the response surface, different approaches can be taken to finding the optimum combination of input variables. The surface can be viewed visually if, as in our case, there are only two input variables. Alternatively, a least squares polynomial fit (usually of low order) can be generated to approximate the response surface, and the minimum found by analytically finding the stationary point(s) by differentiation of the low order polynomials. This simulation runs with the new proposed enrichment function (4.10) with a range of possible s_1 and s_2 values in the range from 0.1 to 2 for both variables and under the same conditions as presented at the beginning of the chapter; densities, gravitational acceleration, absolute permeability, porosity of the medium, dynamic viscosity, pumping rate, and time span and Gauss points to maintain the proposed standard in this research. As it is observed on Figure 5.10, the lowest point on the surface corresponds [1] to s_1 value of 1.2 and s_2 value of 1.1. The values on the table in Figure 5.10 represent the error ϵ_{L^2}. Visually, the lower the error, the more green the colour is presented. As it is observed the higher s goes (on both axis), the colour of the

[1] Notice that these values are only one decimal long for computational effort reasons.

	0.1	0.2	0.3	0.4	0.5	0.6	0.7	0.8	0.9	1	1.1	1.2	1.3	1.4	1.5	1.6	1.7	1.8	1.9	2	s2
0.1	2.0508	12.0695	9.7929	8.8469	10.5094	10.2153	8.9190	9.4773	9.4425	9.4032	9.2304	9.1326	9.8160	10.0151	9.6630	10.0506	10.8804	11.3222	11.5828	11.7292	
0.2	1.8964	11.5445	9.2507	11.1694	5.6703	4.8010	4.7879	5.0036	5.2282	5.3919	5.4816	5.5006	5.4571	5.3620	5.2250	5.0549	4.8604	4.6502	4.4318	4.2114	
0.3	1.8068	0.5881	10.5071	6.8959	3.1614	2.2616	1.9644	1.8730	1.8564	1.8631	1.8748	1.8867	1.8980	1.9086	1.9186	1.9287	1.9393	1.9508	1.9630	1.9760	
0.4	1.7445	0.4242	10.7195	5.6834	2.3612	1.4968	1.1662	1.0226	0.9573	0.9260	0.9091	0.8984	0.8908	0.8851	0.8809	0.8776	0.8749	0.8727	0.8709	0.8693	
0.5	1.6970	0.5591	12.3883	5.1423	1.9878	1.1465	0.8132	0.6568	0.5763	0.5319	0.5051	0.4872	0.4740	0.4633	0.4545	0.4470	0.4407	0.4353	0.4307	0.4265	
0.6	1.6590	0.8184	24.2212	4.8468	1.7844	0.9541	0.6232	0.4644	0.3795	0.3305	0.3002	0.2800	0.2654	0.2542	0.2451	0.2375	0.2311	0.2256	0.2211	0.2185	
0.7	1.6273	0.9839	14.4959	4.6511	1.6651	0.8374	0.5086	0.3506	0.2654	0.2156	0.1845	0.1638	0.1494	0.1387	0.1306	0.1242	0.1191	0.1245	0.1362	0.1480	
0.8	1.6003	1.0911	8.0656	4.4871	1.5930	0.7627	0.4346	0.2780	0.1940	0.1450	0.1146	0.0948	0.0811	0.0715	0.0714	0.0797	0.0905	0.1016	0.1118	0.1209	
0.9	1.5768	1.1614	4.9985	4.3169	1.5490	0.7136	0.3845	0.2292	0.1468	0.0995	0.0714	0.0569	0.0531	0.0567	0.0641	0.0727	0.0811	0.0894	0.0972	0.1045	
1	1.5560	1.2083	3.1552	4.1179	1.5224	0.6812	0.3498	0.1950	0.1148	0.0724	0.0523	0.0470	0.0496	0.0551	0.0615	0.0681	0.0748	0.0815	0.0883	0.0950	
1.1	1.5375	1.2398	1.9705	3.8783	1.5059	0.6601	0.3253	0.1707	0.0939	0.0575	0.0454	0.0457	0.0500	0.0554	0.0611	0.0671	0.0734	0.0798	0.0863	0.0928	
1.2	1.5208	1.2607	1.1979	3.5948	1.4942	0.6472	0.3082	0.1534	0.0799	0.0499	**0.0443**	0.0475	0.0525	0.0581	0.0642	0.0707	0.0774	0.0841	0.0907	0.0972	
1.3	1.5055	1.2742	0.7073	3.2713	1.4832	0.6402	0.2965	0.1410	0.0705	0.0466	0.0459	0.0508	0.0567	0.0634	0.0705	0.0780	0.0854	0.0926	0.0995	0.1062	
1.4	1.4916	1.2825	0.3724	2.9173	1.4693	0.6374	0.2888	0.1321	0.0642	0.0459	0.0485	0.0550	0.0622	0.0702	0.0787	0.0873	0.0955	0.1033	0.1107	0.1177	
1.5	1.4787	1.2869	0.2844	2.5459	1.4493	0.6375	0.2845	0.1260	0.0602	0.0465	0.0517	0.0596	0.0684	0.0778	0.0879	0.0976	0.1066	0.1150	0.1229	0.1302	
1.6	1.4668	1.2886	0.3419	2.1715	1.4204	0.6394	0.2829	0.1219	0.0577	0.0477	0.0549	0.0641	0.0747	0.0857	0.0972	0.1080	0.1179	0.1270	0.1354	0.1431	
1.7	1.4557	1.2882	0.3677	1.8115	1.3802	0.6420	0.2835	0.1197	0.0562	0.0493	0.0581	0.0687	0.0809	0.0937	0.1065	0.1182	0.1290	0.1387	0.1476	0.1557	
1.8	1.4453	1.2862	0.3828	1.4752	1.3270	0.6442	0.2860	0.1193	0.0558	0.0508	0.0611	0.0732	0.0869	0.1014	0.1154	0.1282	0.1397	0.1501	0.1595	0.1682	
1.9	1.4355	1.2831	0.3883	1.1715	1.2598	0.6451	0.2900	0.1206	0.0564	0.0525	0.0638	0.0774	0.0926	0.1089	0.1240	0.1378	0.1501	0.1612	0.1712	0.1803	
2	1.4264	1.2792	0.3881	0.9066	1.1784	0.6435	0.2953	0.1235	0.0580	0.0543	0.0664	0.0813	0.0981	0.1159	0.1323	0.1471	0.1603	0.1720	0.1827	0.1923	
s1	Min val. ϵ_L^2 =		0.0443		Best values																
					s1=	1.2															
					s2=	1.1															

Figure 5.10: Possible combinations for the response surface for ψ^q

table tends to go gradually on a more yellow tone. On experience it has been observed that there is a point on both values of s where the curve behaves in more control. In a different way the lower the values of s indicate a higher level of error as the control is lost. On Figure 5.11 it may be observed the exact point with a red cross where the lowest point of the graph lies. After obtaining the best values for ψ^q we

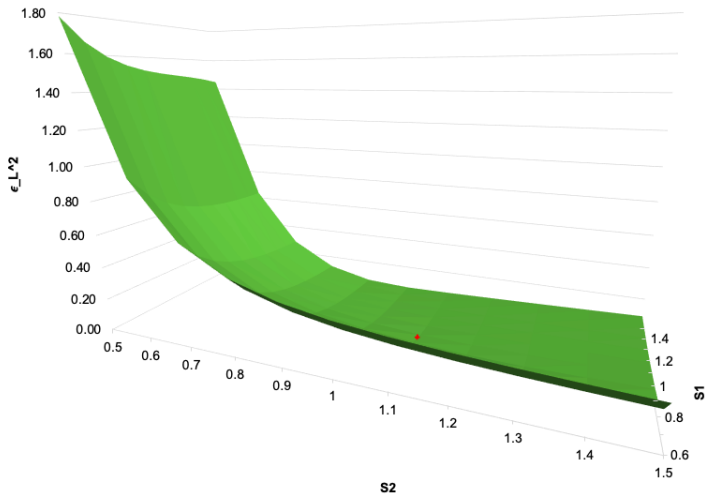

Figure 5.11: Lowest point corresponding s_1 and s_2 response surface for ψ^q

(4.10) can be re-written

$$\psi^q = \mathbf{e}^{-(x/1.2)^{1.1}} \tag{5.2}$$

in order to run further analysis. Figure 5.12 illustrates the distribution of the flux density the model with (5.2) where the resemblance appears to be accurate. Different from the previous (fitted) distribution, a sharp tip in the mid-point of the distribution can be observed, which may result on a sacrifice in error ϵ_{L^2}.

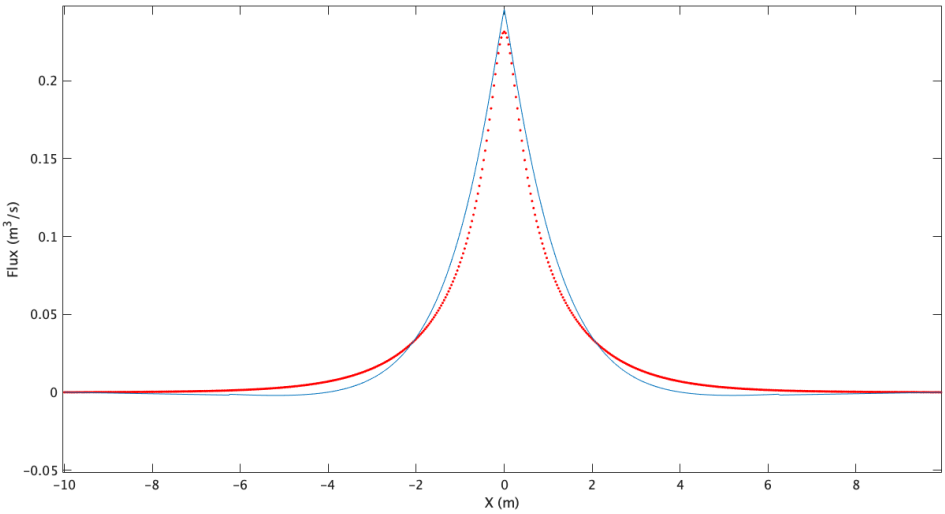

Figure 5.12: Flux density distribution for the modified enrichment function

5.3 Study of different number of Gauss points for numerical integration

Numerical integration lies in the core of all BEM codes. The required order of integration has been well studied for classical formulations in which the integrand contains the well-known product of a low-order polynomial and a fundamental solution. The introduction of enrichment functions means that the integrand may also contain a function of quite arbitrary nature. Indeed, the enriched schemes that work best are those that enrich large elements with problem-dependent functions capturing the essential character of the solution, and those might undergo significant variation over the element. This suggests that further experimentation is required to determine an appropriate integration order for the boundary integrals in the enriched BEM formulations described in this thesis.

In line of pursuing a better cost-effectiveness of higher order numerical integration changes are made to the Gauss-Legendre integration method employed. A range from 6 to 80 Gauss points are studied with the enrichment function (5.1), densities, gravitational acceleration, absolute permeability, porosity of the medium, dynamic viscosity, pumping rate, and time span to maintain the proposed standard in this research. The results on these analyses are shown in Table 5.3 where the left column represents the number of Gauss Points implemented for every test, and the right column reports the error of the L^2 norm ϵ_{L^2} for the corresponding number of Gauss Points included. Figure 5.13 represents the behaviour of the error of the L^2 norm ϵ_{L^2} in the y-axis against the different scenarios where the number of Gauss Points changes. This is useful as evidence on how changes to the number of Gauss Points to the model would affect the fidelity of the model.

5.4 Different problem conditions

As the tests for a single exponential equation are presented, other approaches seem to be appropriate to evaluate such as different heights with this single exponential equation. The model's enrichment function and conditions for this approach are as stated at the beginning of the chapter i.e. enrichment function (5.1), densities, gravitational acceleration, absolute permeability, porosity of the medium, dynamic viscosity, time span and Gauss points. The same values are kept for most of the simulations to maintain

Gauss Points	Error of the L^2 norm ϵ_{L^2}
6	4.2625 %
8	4.3612 %
10	4.4305 %
20	4.5746 %
30	4.6259 %
40	4.6522 %
50	4.6679 %
60	4.6785 %
70	4.6860 %
80	4.6916 %

Table 5.3: Results from Study of error ϵ_{L^2} with different Gauss Points

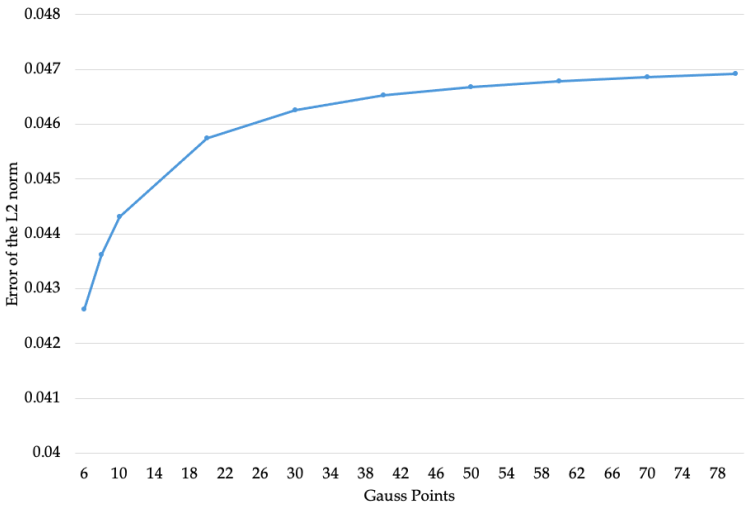

Figure 5.13: Analysis of error ϵ_{L^2} with different Gauss Points

a standard in this research; however, for the first time a physical condition is changed, in this case the height of the pumping sink is studied.

5.4.1 Different heights

The study of a new focus is now simulated and tested as one of the goals of this research is to apply the enrichment scheme on the model with changes on physical conditions. Here the position of the pump is modified in a varied range of heights between coordinates (0,2.5) to (0,3.5) stepping in the y-coordinates 0.1 metres and the error of the L^2 norm ϵ_{L^2} is measured. The values to measure for this test include for every height of the pumping sink a) height of the interface at the mid-point; b) Total flux of the interface Q_Γ and c) relative error of the L^2 norm ϵ_{L^2}.

Height of the pump $(y-coord)$	**Maximum height** $[m]$	$\mathbf{Q_\Gamma}$ $[m^3/s]$	$\epsilon_{\mathbf{L^2}}$
2.5	2.4309	0.4836	0.312
2.6	2.3724	0.4869	0.2043
2.7	2.3349	0.4886	0.1356
2.8	2.307	0.4897	0.094
2.9	2.2851	0.4906	0.0649
3	2.2674	0.4913	0.051
3.1	2.253	0.4919	0.0648
3.2	2.2413	0.4924	0.0794
3.3	2.2318	0.4928	0.0932
3.4	2.2245	0.4932	0.1065
3.5	2.2194	0.4936	0.1203

Table 5.4: Results from different pump heights

The results obtained are presented in Table 5.4 where an increment on the total flux Q_Γ can be appreciated. In Figure 5.14 it is appreciated the how Total flux Q_Γ for every position the tendency is

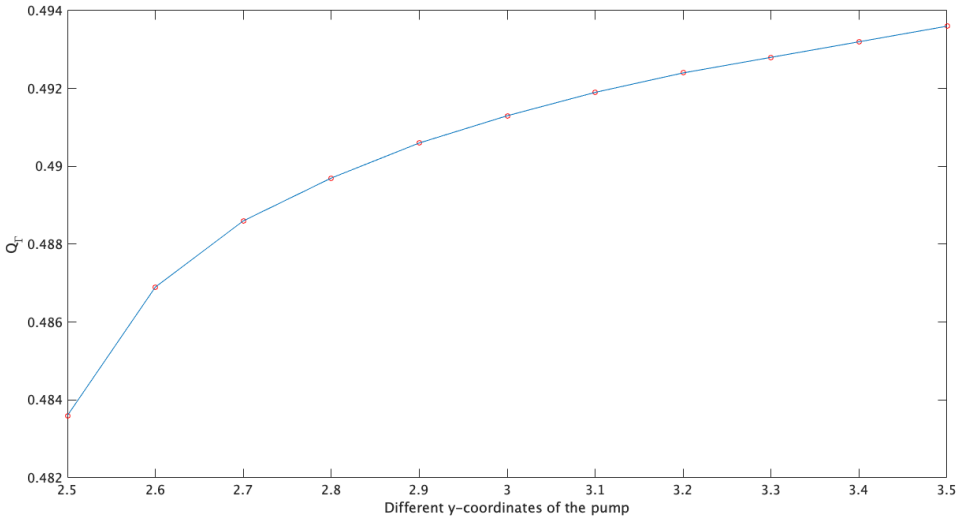

Figure 5.14: Analysis of the Total flux Q_Γ where y-coordinates $\in [1.5, 3.5]$

of growth. It is quite noticeable the increment on Total flux Q_Γ as the pump becomes higher, however, the author must not take only this variable in consideration as experience indicates that other indicators can help to determine if the changes are effective or not. This leads to the analysis of the error of the L^2 norm ϵ_{L^2}.

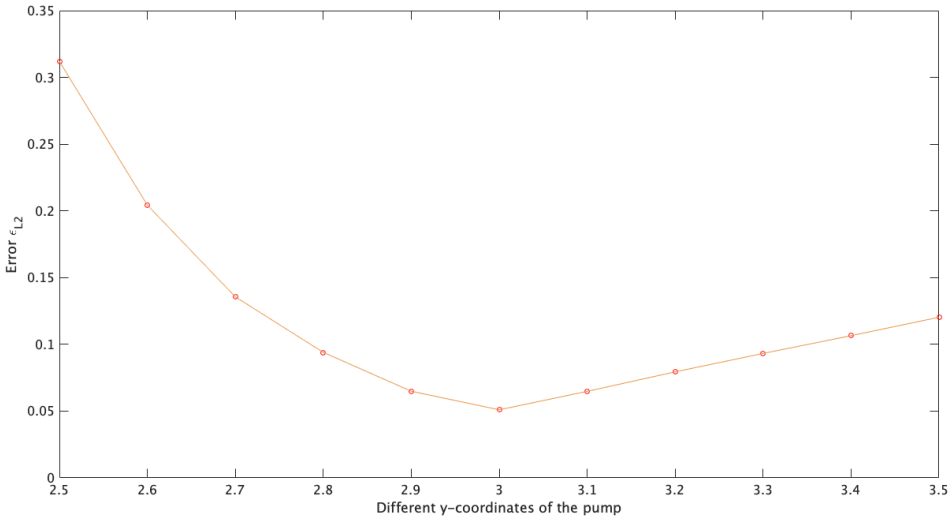

Figure 5.15: Analysis of the error of the L^2 norm ϵ_L^2 where y-coordinates $\in [1.5, 3.5]$

Results from 5.15 reveal that the least relative error of the L^2 norm ϵ_L^2 is the original pump position. This is not surprising as the enrichment function used was designed using the results of a model with the pump in this position. It is also very interesting to see that as high as the Total flux Q_Γ may appear in Figure 5.14, the results from 5.15 suggest that a position above 3 involves a higher level of error.
To explain in a more illustrative way this relationship between flux-error, Figure 5.16 presents a set of plots (one for every pump position) where the red curves represent the reference solutions (i.e. results from an un-enriched refined model) against the results from this research represented by a blue line with amber markings. It is evident that for low pump heights, where the pump is close to the interface, the flux density distribution exhibits a sharp peak that the exponential enrichment function is unable to resolve accurately. It should be recalled that the results of the enriched scheme (blue lines) are produced by a model with only 9 degrees of freedom on the interface. Notice the resemblance between reference solution and result as the relative error of the L^2 norm ϵ_L^2 is lower.

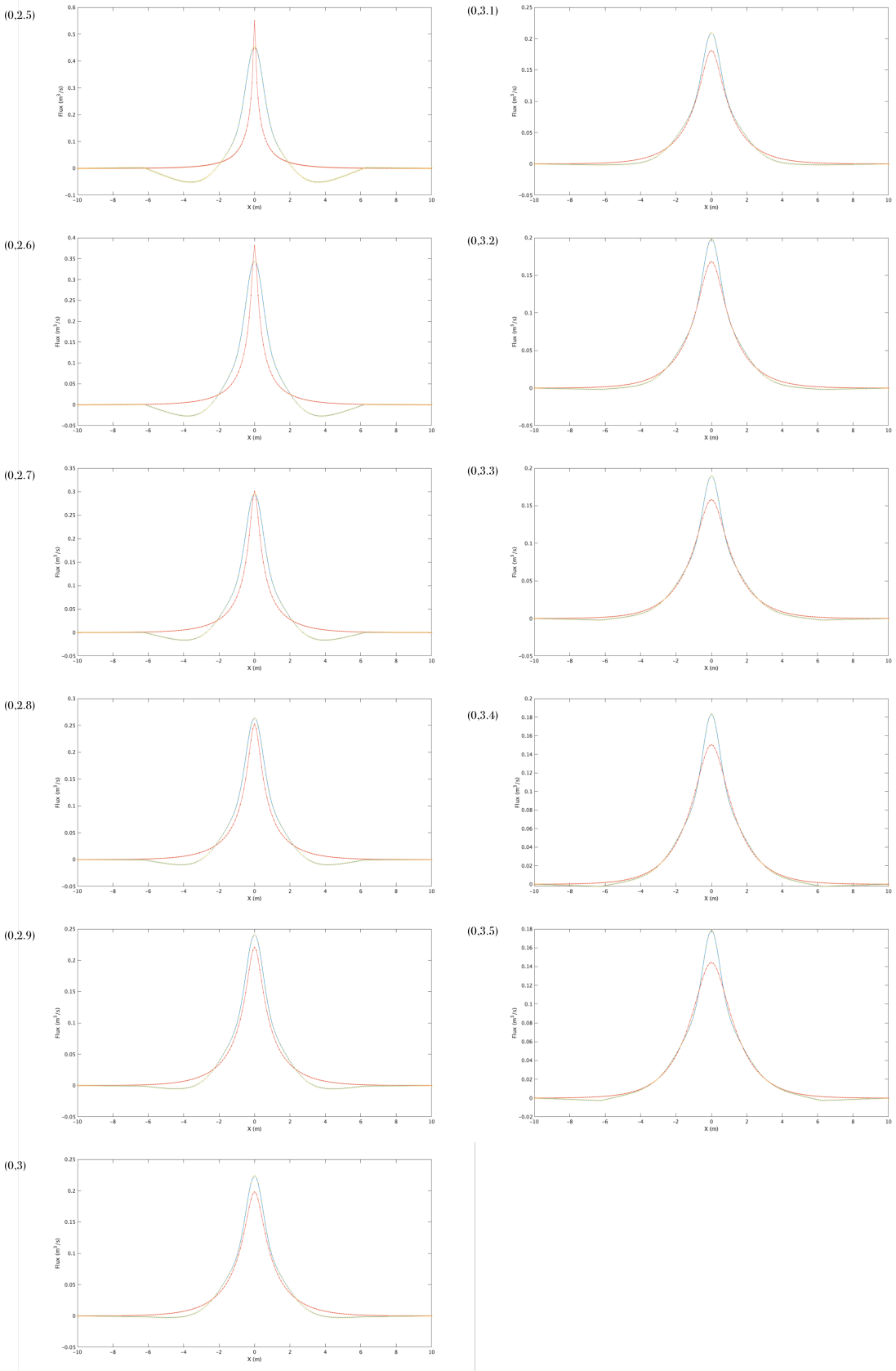

Figure 5.16: Flux density distribution for different pump locations in a range of y-coordinates from 2.5 to 3.5

On the contrary, the greater the error, the more distorted the relation. Figure 5.17 illustrates the

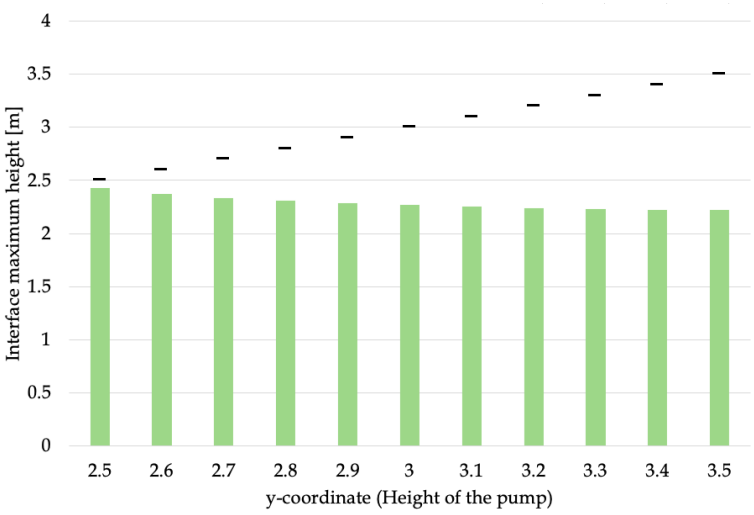

Figure 5.17: Analysis of the Tip height $[m]$ with different pump heights and and pump different rates

relationship on how far the maximum value of the height of the interface gets compared to the position of the pump.

5.4.2 Different heights and variable s

In the previous sections of this chapter, a variety of tests have been performed and obtained good results comparing two metrics (i.e. Q_Γ and ϵ_{L^2}); nonetheless, the relative error of the L^2 norm ϵ_{L^2} has demonstrated to be more reliable over the previous tests. For this reason, a visual analysis has been produced to observe the behaviour of the relative error of the L^2 norm ϵ_{L^2} in different pump heights as s is varied in a range from 0.5 to 3. Figure 5.18 shows the variation in the relative L^2 error norm against s.

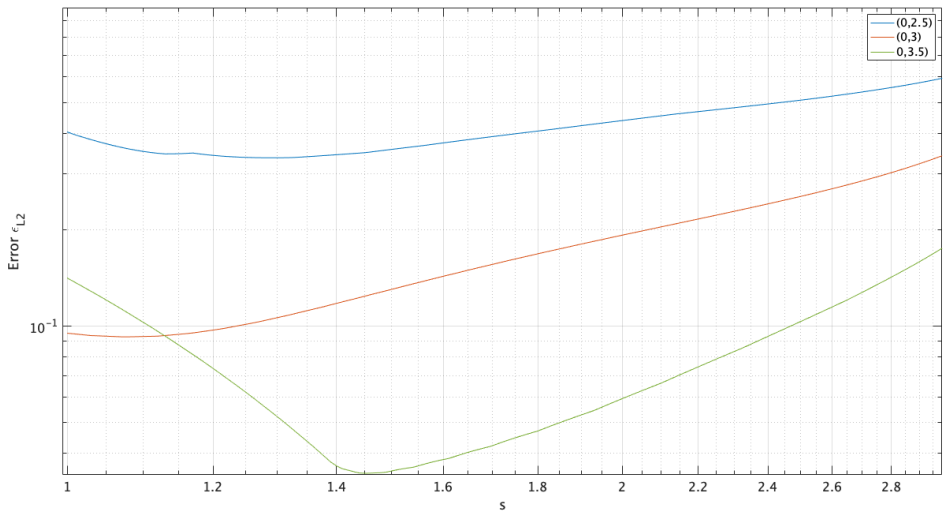

Figure 5.18: Analysis of ϵ_{L^2} with different pump heights and pump rate of $-1.5 \times 10^{-3}[m^3/s]$

In this case three behaviour lines can be observed, one for every height of the pumping sink changed in the geometry of the model. The blue line represents the error of the L^2 norm values for a simulation where the pump height had been modified to be of coordinates $(0, 2.5)$. This means that the elevation of the

pump was 0.5 metres lower than the original coordinates $(0, 3)$ represented with the orange line. In the same manner the green line represents the error values for a simulation with 0.5 metres above the original leaving coordinates $(0, 3.5)$. It is evident that the lower errors are found for the larger pump heights, a result that is suggested by the difficulty of resolving the sharp peak in the flux density distribution for y=2.5 m as seen in 5.16.

5.5 Stop at different time steps

Besides the physical variables that compose any model, time-dependent analyses usually consider evaluation and evolution of the model for every time step; in this thesis, a time step 20 has been utilised to monitor each test; however insightful results are obtained by performing simulations stopping at time step 20, 19, 10 and 5. Two sets of insightful results are obtained for both the simulation conditions include the specified enrichment function and physical conditions as stated at the beginning of the chapter i.e. enrichment function (5.1), densities, gravitational acceleration, absolute permeability, porosity of the medium, dynamic viscosity, and Gauss points. For the first set, the location of the pump is (0,2.5) thus, 0.5 metres below the original pumping sink and with a pumping rate of $-1.5 \times 10^{-3}[m^3/s]$. It can be

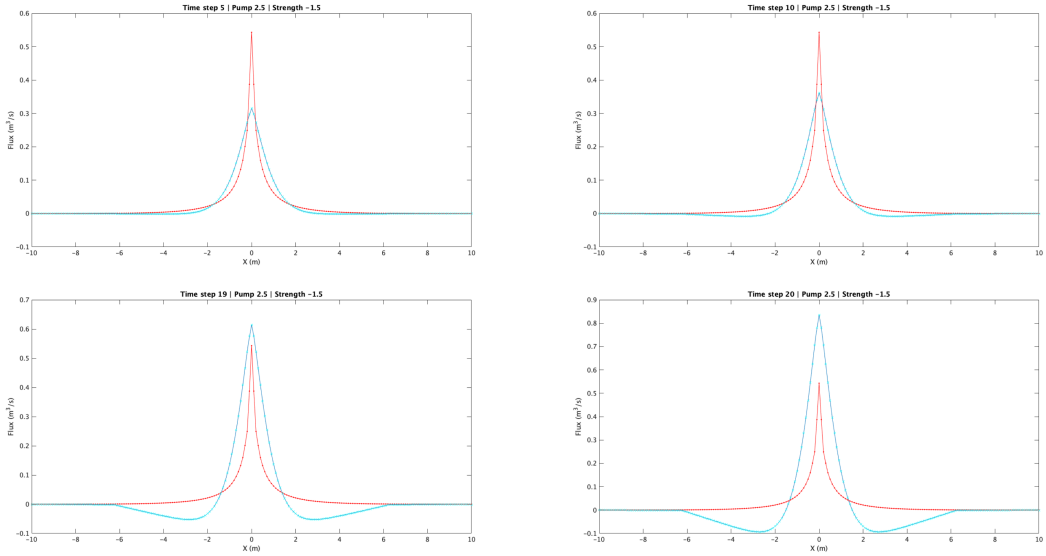

Figure 5.19: Flux density distribution for different time steps at pump location $(0, 2.5)$ and pump strength of -1.5

observed in Figure 5.19 at an early time step 5 the blue distribution does not quite reach the height of the reference solution in red, although the shape of the distribution is very similar. As time step increase to 10, the flux density begins to rise but still maintaining a similar distribution shape. Nonetheless, it can be observed that by time steps 19 and 20 the flux density has over passed the reference solution and evolved into a distorted distribution resulting in a large error of the L^2 norm.
In second set, the location of the pump is changed to (0,3.5) thus, 0.5 metres above the original pumping sink and with a pumping rate of $-1.5 \times 10^{-3}[m^3/s]$. Figure 5.20 at an early time step 5 the blue distribution raised above the reference solution in red. As time step increase to 10, a clear change cannot be observed compared to time step 5. Time steps 19 and 20 show that the flux density has not passed the reference solution and the distribution resembles the reference solution quite nicely, meaning that the error that is produced at this particular pump height is produced due to this peak that is consequence of the enrichment function selected.

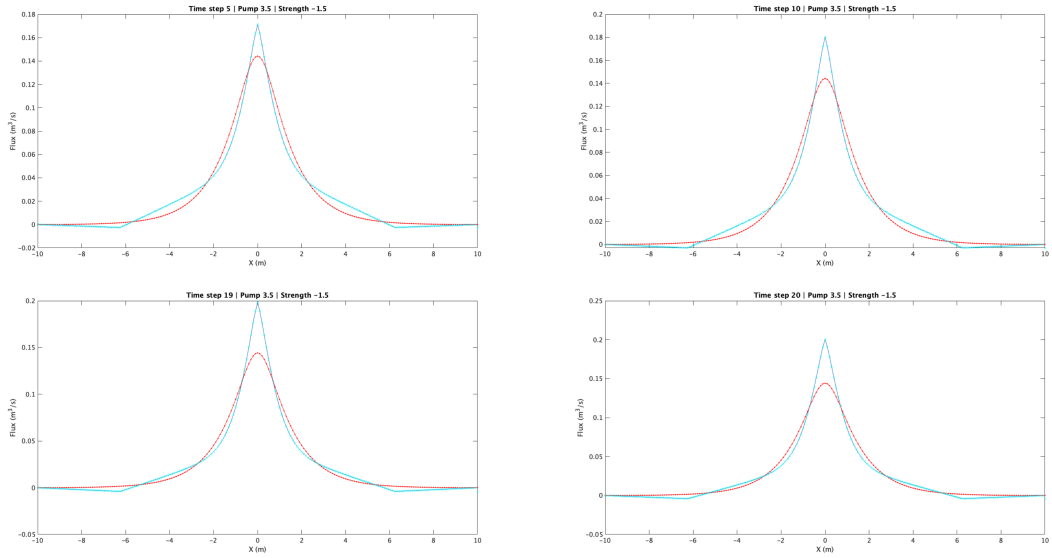

Figure 5.20: Flux density distribution for different time steps at pump location $(0, 3.5)$ and pump strength of -1.5

5.6 Change in the shape of the geometry

A fourth simulation with changes on the physical aspect of the model is presented in this section. The model's enrichment function and conditions for this approach are also as stated at the beginning of the chapter i.e. enrichment function (5.1), densities, gravitational acceleration, absolute permeability, porosity of the medium, dynamic viscosity, time span, Gauss points and position of the pump; the different physical condition in this test is the geometry. A linear-boundary geometry 2.1 was originally proposed by the work presented by Gontijo et. al. [2] which has been adopted in the previous simulations in this thesis. The simulation performed in this section now adopts a new geometry as seen in Figure 4.5 described at the end of section 4.4. In this simulation, focus is given to the following measures: a) height of the interface at the mid-point; b) Total flux of the interface Q_Γ and c) relative error of the L^2 norm ϵ_{L^2}.

The results obtained are presented in Table 5.5 and the distribution of the flux density can be observed

Maximum height $[m]$	$\mathbf{Q_\Gamma}$ $[m^3/s]$	$\boldsymbol{\epsilon_{L^2}}$
2.2061	0.3236	0.0379

Table 5.5: Results from different geometry

in Figure 5.21. The distribution of both reference solution and enriched scheme version has changed as geometry has changed both in area and shape. It can also be appreciated that the resemblance between both distributions is successfully similar in accordance with the error of the L^2 norm ϵ_{L^2} presented in Table 5.5.

5.7 Combination from the best results

Finally, a simulation is produced combining all of the best results from the previous simulations and analysis. The adopted conditions to do this are as follow: a) equal densities $\rho_1 = \rho_2 = 1000[kg/m^3]$; b) gravitational acceleration of g is of 9.81 $[m/s^2]$; c) absolute permeability k of 1 [darcy]; d) porosity of medium θ of 1; and e) dynamic viscosity for both zones $\mu_{1,2}$ of 0.001; f) constant pumping rate of

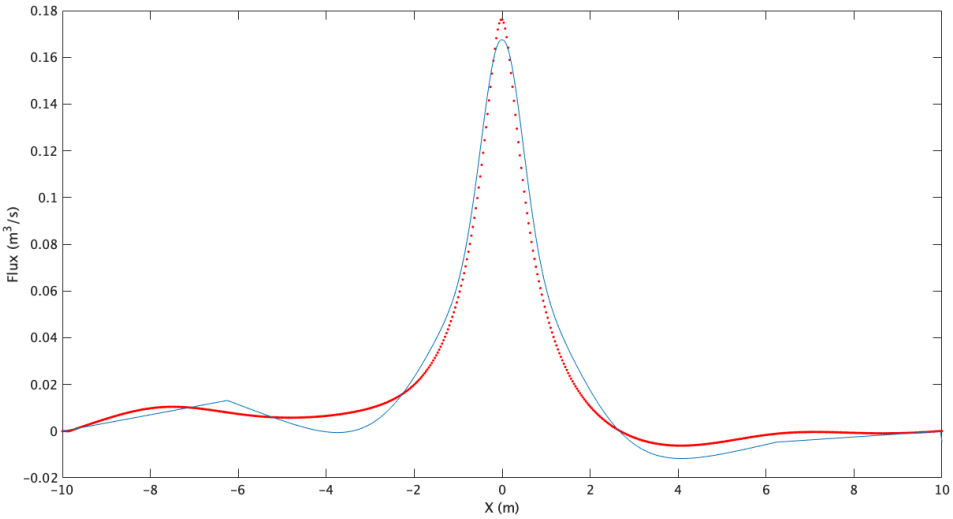

Figure 5.21: New geometry distribution

$-1.5 \times 10^{-3}[m^3/s]$; g) model stopped after 20 time steps with a time span of $2.67[s]$ per time step; h) 30 Gauss Points; i) pump location (0,3). With j) collocation point strategy (f); and k)and enrichment function (5.2).

In a similar basis as the previous simulation in section 5.6, the values to measure include a) height of the interface at the mid-point; b) Total flux of the interface Q_Γ and c) relative error of the L^2 norm ϵ_{L^2}. The

Maximum height $[m]$	$\mathbf{Q_\Gamma}$ $[m^3/s]$	$\epsilon_{\mathbf{L^2}}$
2.2237	0.3227	0.0397

Table 5.6: Results from combined strategies

results obtained are presented in Table 5.6 and the distribution of the flux density can be observed in the next chapter. In this simulation the resemblance between reference solution and enriched scheme version is indeed very similar just as presented in the previous simulation. The differences vary in accordance with the error of the L^2 norm $\epsilon_{\mathbf{L^2}}$ presented in Table 5.6.

Chapter 6

Conclusions

An enriched boundary element scheme to improve computational efficiency in modelling the water coning problem has been investigated in a way that the author can be sure that work for different conditions. The findings on these test simulations indicate the way in which accuracy on the results is not compromised in order to further research a 3D model.

As the Total flux Q_Γ is quick and easy to code, the author becomes aware that this in fact is a poor metric in the sense that it may indicate great results when in fact the results are really not very good. A good compliment to measure the performance of the simulation tested is the relative error of the L^2 norm ϵ_{L^2} as it compares the result against a reference solution that is obtained from the classical refined Boundary Element Method (BEM) model. This is very useful when the best results of Q_Γ are not fully reliable as the shape of the flux density in the model is may not be as expected.

The Additional Collocation Point (ACP) strategy conducted in 5.1 evidences that by adding collocation points the enriched scheme is complemented, but increasing these collocation points, the number of equations that reveal information in the model increases as well giving more clarity in the information from the simulation; specially when these are included in the interface that is where the enrichment takes place and it is also where the effect of the pumping sink is reproduced. Apparently this strategy helps with the improvement of the model it can be observed that the calculated Total flux Q_Γ increases. Nonetheless, a correlation analysis between Total flux Q_Γ and the relative error of the L^2 norm ϵ_{L^2} is conducted revealing that these results show that the more points are included, the better the results obtained. However, it has to be kept in mind that the more ACPs included, the more computational effort it will take to run any simulation and may have an impact on the error produced. In this case, having added six ACPs besides the three that are required yields better information without sacrificing a great deal of processing time or significant increase in error. With this in mind, strategy 'f' results being the best as presented in Section 4.4.

The first set of modifications in Section 5.2 consisted on reducing the function and instead of having a function composed by two exponential equations, now it is a single exponential equation that consists of a coefficient s and an exponent to the second power (square). This coefficient s was tested in a range $s \in [1/5, 3]$ in order to find a value that yielded a better Total flux Q_Γ and the results demonstrated that the higher s was selected, the broader the flux density distribution along the interface becomes, thus, obtaining a higher Total flux Q_Γ. In another perspective, the relative error of the L^2 norm ϵ_{L^2} was also produced. Graphically, it can be appreciated as the coefficient s becomes closer to 1, the less error the model yields. Analysing the relative error of the L^2 norm ϵ_{L^2} helped the author notice that for this model, when the Total flux Q_Γ is good, but the relative error of the L^2 norm ϵ_{L^2} is high, it is because the

model does not have enough information to deal with these results, so it is better to keep the simulations open for new approaches. The second set of modifications keeps the same coefficient (now called s_1) and implicated that the exponent of the enriched flux density equation (now called s_2) could be modified to fit better the behaviour of the reference solution. Two tests performed also in a range $s_1 \in [1/5, 3]$ and with two different $s_2 = 1.2$ and $s_2 = 1.2$. The results indicate a similar behaviour between both models, however, the analysis suggests that a lower error is produced when s_1 becomes closer to 1. This arises questions and a response surface model testing this modified enrichment function yields optimum values of $s_1 = 1.2$ and $s_2 = 1.1$ With a small relative error of the L^2 norm $\epsilon_{L^2} < 5\%$.

Increasing the number of Gauss Points selected to evaluate the model as shown in Section 5.3 does give a reliable result on the accuracy of the error of the L^2 norm ϵ_{L^2} as it reaches an asymptotic behaviour as the number of Gauss Points becomes higher. Although a horizontal tendency goes smoothly as the number of Gauss Points increase over 20 points, the benefit of increasing this numbers is not enough to implement this change. Contrarily, as the number of Gauss Points decreases, a drop on the curve evidences the unreliability of decreasing the number of Gauss Points. It is then not recommendable to change the number of Gauss Points as no real benefit is obtained and it has been proven that the variation when increasing the number of Gauss Points is no greater than 0.03%.

Section 5.4 presents a variety of tests and information on whether to change some of the physical conditions of the model to increase the oil production. In this case, the pump position is changed in the geometry without leaving the oil zone (pumping zone). The results show good results when the Total flux Q_Γ is assessed however, relative error of the L^2 norm ϵ_{L^2} indicate a high error as the pump position moves away from the original pump at (0,3). This behaviour can be well explained as the distributions of the flux density for every pump position reveal that the model may not have enough information to model other pump heights. It is important to point out at this stage that the optimal s for different pump heights follows the general picture of a steeper Gaussian enrichment function being better for the low pump heights where the flux density distribution is steeper. It should be noted as well that even when the pump height is modified, the premise of the interface not reaching the pump is fulfilled. Subsection 5.4.2 helps to understand the behaviour of the relative error of the L^2 norm ϵ_{L^2} as s varies on different positions. As expected, the higher the pump, the lower the relative error of the L^2 norm ϵ_{L^2} would be generally.

Section 5.5 analyses the behaviour of the model by stopping the pump at given time steps as a consequence of the results obtained in 5.16. Results show that in an early stage, a resemblance with the reference solution is acceptable, but with time, a distortion in the flux density distribution over the interface is produced meaning that for these particular changes in the model, the enrichment function works but is not as accurate as expected.

In Section 5.6 the upper and lower boundaries of the geometry of the model is modified and the results indicate a good performance of the model in this case yielding a relative error of the L^2 norm $\epsilon_{L^2} < 4\%$ and a distribution that resembles nicely the reference solution.

Finally, when the best ACP strategy, new enrichment function, Gauss points selected, best pump position and time step meet, the variation between the results is less than 1% in error as presented. This concludes that the model can be simplified and still reach accurate results in certain different conditions such as different geometry.

Model	**Maximum height** $[m]$	$\mathbf{Q_\Gamma}$ $[m^3/s]$	$\epsilon_{\mathbf{L^2}}$
Original	2.2674	0.4913	0.0431
Combined strategies	2.2237	0.3227	0.0397

Table 6.1: Original enriched model vs. Combined strategies model

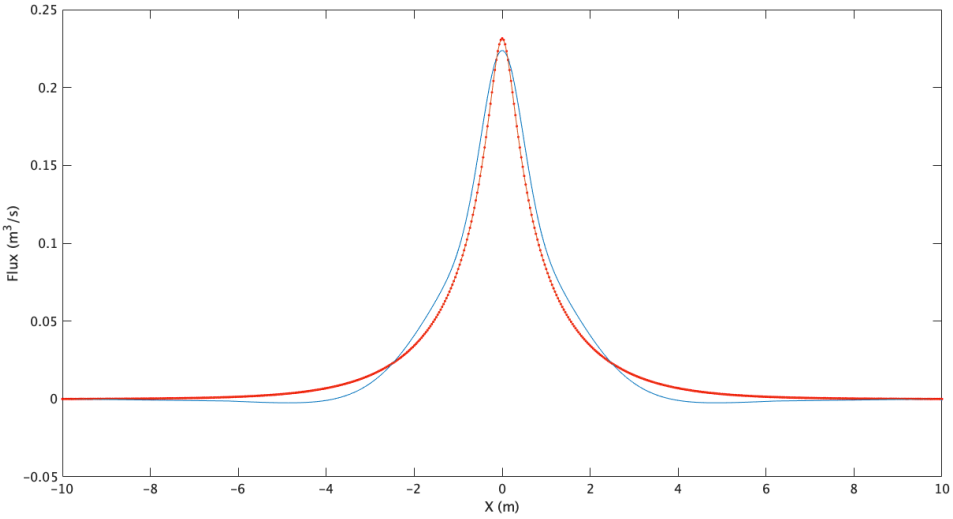

Figure 6.1: Flux density distribution for the original enriched model

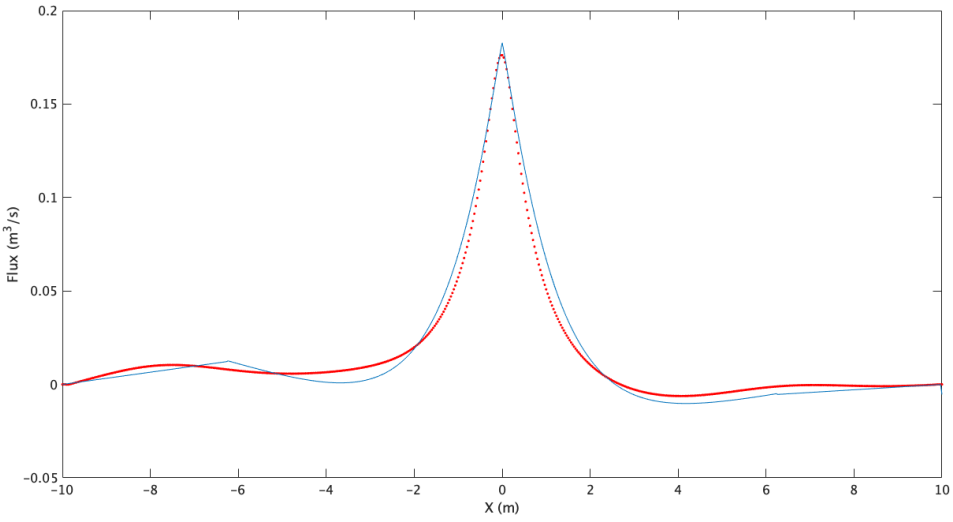

Figure 6.2: Flux density distribution for combined strategies

References

[1] J. Trevelyan, *Boundary Elements for Engineers: Theory and Applications*. Computational Mechanics Publications, 1994.

[2] G. Gontijo, E. Albuquerque, and E. Fortaleza, "Study on the water coning phenomenon in oil wells using the boundary element method," in *International conference on boundary element techniques, Florence, Italy*.

[3] J. M. Ruiz, B. Chen, J. Trevelyan, P. Gourgiotis, E. Albuquerque, and C. U. D. Ribeiro, "Enriched bem for water coning," *Methods UKBIM12*, p. 41, 2019.

[4] J. Bear, *Dynamics of fluids in porous media*. Courier Corporation, 2013.

[5] M. Muskat, *Physical principles of oil production*. McGraw-Hill Book Co., 1949.

[6] M. Muskat and R. D. Wycokoff, "An approximate theory of water-coning in oil production," *Transactions of the AIME*, vol. 114, no. 01, pp. 144–163, 1935.

[7] L. A. Høyland, P. Papatzacos, and S. M. Skjaeveland, "Critical rate for water coning: Correlation and analytical solution," *SPE Reservoir Engineering*, vol. 4, no. 04, pp. 495–502, 1989.

[8] S. K. Lucas, J. R. Blake, and A. Kucera, "A boundary-integral method applied to water coning in oil reservoirs," *The Journal of the Australian Mathematical Society. Series B. Applied Mathematics*, vol. 32, no. 3, pp. 261–283, 1991.

[9] R. MacDonald, "Methods for numerical simulation of water and gas coning," *Society of Petroleum Engineers Journal*, vol. 10, no. 04, pp. 425–436, 1970.

[10] J. Bear and G. Dagan, "Some exact solutions of interface problems by means of the hodograph method," *Journal of Geophysical Research (1896-1977)*, vol. 69, no. 8, pp. 1563–1572, 1964.

[11] N. Al-Afaleg and I. Ershaghi, "Coning phenomena in naturally fractured reservoirs," in *SPE Western Regional Meeting*, vol. All Days, (SPE-26083-MS).

[12] S. K. Lucas and A. Kucera, "A boundary integral method applied to the 3d water coning problem," *Physics of Fluids*, vol. 8, no. 11, pp. 3008–3022, 1996.

[13] J. E. Farmen, G. Wagner, U. Oxaal, P. Meakin, J. Feder, and T. Jøssang, "Dynamics of water coning," *Physical review. E, Statistical physics, plasmas, fluids, and related interdisciplinary topics*, vol. 60, no. 4 Pt B, p. 4244, 1999.

[14] H. Bahrami, S. R. Shadizadeh, and I. Goodarzniya, "Numerical simulation of coning phenomena in naturally fractured reservoirs," *Technology*, vol. 23, p. 25, 2004.

[15] E. Pérez-Martinez, F. Rodriguez-de la Garza, and F. Samaniego-Verduzco, "Water coning in naturally fractured carbonate heavy oil reservoir – a simulation study," in *SPE Latin America and Caribbean Petroleum Engineering Conference*, vol. All Days, (SPE-152545-MS).

[16] R. A. Azim, "Evaluation of water coning phenomenon in naturally fractured oil reservoirs," *Journal of Petroleum Exploration and Production Technology*, vol. 6, no. 2, pp. 279–291, 2016.

[17] M. S. Mohamed, M. Seaid, J. Trevelyan, and O. Laghrouche, "An enriched finite element model with q-refinement for radiative boundary layers in glass cooling," *Journal of Computational Physics*, vol. 258, pp. 718 – 737, 2014.

[18] J. M. Melenk and I. Babuška, "The partition of unity finite element method: basic theory and applications," in *Research Report/Seminar für Angewandte Mathematik*, vol. 1996, Eidgenössische Technische Hochschule, Seminar für Angewandte Mathematik.

[19] N. Moës, J. Dolbow, and T. Belytschko, "A finite element method for crack growth without remeshing," *International journal for numerical methods in engineering*, vol. 46, no. 1, pp. 131–150, 1999.

[20] O. C. Zienkiewicz, *The finite element method for fluid dynamics*. Oxford: Oxford : Butterworth-Heinemann, 6th ed. ed., 2005.

[21] G. de Vries and D. H. Norrie, "The application of the finite-element technique to potential flow problems," *Journal of Applied Mechanics*, vol. 38, no. 4, pp. 798–802, 1971.

[22] A. J. Deeks and L. Cheng, "Potential flow around obstacles using the scaled boundary finite-element method," *International journal for numerical methods in fluids*, vol. 41, no. 7, pp. 721–741, 2003.

[23] A. A. Becker, *The boundary element method in engineering : a complete course*. London ; New York: McGraw-Hill, 1992.

[24] Y. Liu and T. Rudolphi, "Some identities for fundamental solutions and their applications to weakly-singular boundary element formulations," *Engineering analysis with boundary elements*, vol. 8, no. 6, pp. 301–311, 1991.

[25] O. Laghrouche, P. Bettess, and R. Astley, "Modelling of short wave diffraction problems using approximating systems of plane waves," *International Journal for Numerical Methods in Engineering*, vol. 54, no. 10, pp. 1501–1533, 2002.

[26] S. Chandler-Wilde, I. G. Graham, S. Langdon, and E. A. Spence, "Numerical-asymptotic boundary integral methods in high-frequency acoustic scattering," *Acta numerica*, vol. 21, pp. 89–305, 2012.

[27] B. Gilvey, J. Trevelyan, and G. Hattori, "Singular enrichment functions for helmholtz scattering at corner locations using the boundary element method," *International Journal for Numerical Methods in Engineering*, vol. 121, no. 3, pp. 519–533, 2020.

[28] P. O'Hara, C. Duarte, and T. Eason, "Generalized finite element analysis of three-dimensional heat transfer problems exhibiting sharp thermal gradients," *Computer Methods in Applied Mechanics and Engineering*, vol. 198, no. 21-26, pp. 1857–1871, 2009.

[29] P. O'Hara, C. A. Duarte, and T. Eason, "Transient analysis of sharp thermal gradients using coarse finite element meshes," *Computer Methods in Applied Mechanics and Engineering*, vol. 200, no. 5-8, pp. 812–829, 2011.

[30] G. C. Diwan, M. S. Mohamed, M. Seaid, J. Trevelyan, and O. Laghrouche, "Mixed enrichment for the finite element method in heterogeneousmedia," *International Journal for Numerical Methods in Engineering*, vol. 101, no. 1, pp. 54–78, 2015.

[31] E. Perrey-Debain, J. Trevelyan, and P. Bettess, "Wave boundary elements: a theoretical overview presenting applications in scattering of short waves," *Engineering analysis with boundary elements*, vol. 28, no. 2, pp. 131–141, 2004.

Appendix A

Appendix

A.1 Trapezium rule to obtain Q

This function was employed in the code to obtain the total flux Q which comes from a numerical integration of the area under the flux density curve along the interface trough the trapezium rule.

$$Q = \int_{\Gamma_0}^{\Gamma_n} q \, d\Gamma = \frac{1}{2} h \left[(y_0 + y_n) + 2(y_1 + y_2 + y_3 + ... + y_{n-1}) \right]$$

where the ys represent the sides of the trapeziums formed along the interface and the h represents the width of each trapezium.

A.2 REL2

This function was employed in the code to obtain the Relative Error of the L2 Norm at the maximum height of the oil-water interface.

$$REL2 = \frac{\sqrt{\int_{\Gamma_{ow}} (q - q^{ref})^2 \, d\Gamma}}{\sqrt{\int_{\Gamma_{ow}} (q^{ref})^2 \, d\Gamma}}$$